

Complex refractive indices and single scattering albedo of global dust aerosols in the shortwave spectrum and relationship to size and iron content

Claudia Di Biagio¹, Paola Formenti¹, Yves Balkanski², Lorenzo Caponi^{1,3}, Mathieu Cazaunau¹, Edouard Pangui¹, Emilie Journet¹, Sophie Nowak⁴, Meinrat O. Andreae^{5,6}, Konrad Kandler⁷, Thuraya Saeed⁸, Stuart Piketh⁹, David Seibert¹⁰, Earle Williams¹¹, and Jean–Francois Doussin¹

¹ LISA, UMR CNRS 7583, Université Paris–Est–Créteil, Université de Paris, Institut Pierre Simon Laplace (IPSL), Créteil, France

² Laboratoire des Sciences du Climat et de l'Environnement, CEA CNRS UVSQ UP Saclay, 91191, Gif sur Yvette, France

³ PM_TEN srl, Piazza della Vittoria 7/14, 16121, Genoa, Italy

⁴ Plateforme RX UFR de chimie, Université Paris Diderot, Paris, France

⁵ Max Planck Institute for Chemistry, P.O. Box 3060, 55020, Mainz, Germany

⁶ Geology and Geophysics Department, King Saud University, Riyadh, Saudi Arabia

⁷ Institut für Angewandte Geowissenschaften, Technische Universität Darmstadt, Schnittspahnstr. 9, 64287 Darmstadt, Germany

⁸ Science Department, College of Basic Education, Public Authority for Applied Education and Training, Al–Ardeya, Kuwait

⁹ Climatology Research Group, Unit for Environmental Science and Management, North–West University, Potchefstroom, South Africa

¹⁰ Walden University, Minneapolis, Minnesota, USA

¹¹ Parsons Laboratory, Massachusetts Institute of Technology, Cambridge, Massachusetts, USA

Correspondence to: C. Di Biagio (claudia.dibiagio@lisa.u-pec.fr)

Abstract

The optical properties of airborne mineral dust depend on its mineralogy, size distribution, and shape, and might vary between different source regions. To date, large differences in refractive index values found in the literature have not been fully explained. In this paper we present a new dataset of complex refractive indices ($m=n-ik$) and single scattering albedos (SSA) for 19 mineral dust aerosols over the 370–950 nm range in dry conditions. Dust aerosols were generated from natural parent soils from eight source regions (Northern Africa, Sahel, Middle East, Eastern Asia, North and South America, Southern Africa, and Australia). They were selected to represent the global scale variability of the dust mineralogy. Dust was re-suspended into a 4.2 m³ smog chamber where its spectral shortwave scattering (β_{sca}) and absorption (β_{abs}) coefficients, number size distribution, and bulk composition were measured. The complex refractive index was estimated by Mie calculations combining optical and size data, while the spectral SSA was directly retrieved from β_{sca} and β_{abs} measurements. Dust is assumed to be spherical in the whole data treatment, which introduces a potential source of uncertainty. Our results show that the imaginary part of the refractive index (k) and the SSA vary widely from sample to sample, with values for k in the range 0.0011 to 0.0088 at 370 nm, 0.0006 to 0.0048 at 520 nm, and 0.0003 to 0.0021 at 950 nm, and values for SSA in the range 0.70 to 0.96 at 370 nm, 0.85 to 0.98 at 520 nm, and 0.95 to 0.99 at 950 nm. In contrast, the real part of the refractive index (n) is mostly source (and wavelength) independent, with an average value between 1.48 and 1.55. The sample-to-sample variability in our dataset of k and SSA is mostly related to differences in the dust's iron content. In particular, a wave-

45 length-dependent linear relationship is found between the magnitude of k and SSA and the mass con-
46 centrations of both iron oxide and total elemental iron, with iron oxide better correlated than total ele-
47 mental iron to both k and SSA. The value of k was found to be independent of size. When the iron oxide
48 content exceeds 3%, the SSA linearly decreases with increasing fraction of coarse particles at short
49 wavelengths (< 600 nm).

50 Compared to the literature, our values for the real part of the refractive index and SSA are in line with
51 past results, while we found lower values of k compared to most of the literature values currently used
52 in climate models

53 We recommend that source-dependent values of the SW spectral refractive index and SSA be used in
54 models and remote sensing retrievals instead of generic values. In particular, the close relationships
55 found between k or SSA and the iron content in dust enable establishing predictive rules for spectrally-
56 resolved SW absorption based on particle composition.

57

58 **Introduction**

59 With teragram amounts of annual emissions, a residence time of about 1–2 weeks in the atmosphere,
60 and a planetary-scale transport, mineral dust aerosols are a global phenomenon (Uno et al., 2009;
61 Ginoux et al., 2012), and contribute significantly to the global and regional aerosol loading (Ridley et
62 al., 2016) and direct radiative effect (Miller et al., 2014).

63 However, large uncertainties still persist on the magnitude and overall sign of the dust direct radiative
64 effect (Boucher et al., 2013; Highwood and Ryder, 2014; Kok et al., 2017). One of the major sources of
65 this uncertainty is our insufficient knowledge of the dust's absorption properties in the shortwave (SW)
66 and longwave (LW) spectral ranges (e.g., Balkanski et al., 2007; Samset et al., 2018), given that mineral
67 dust contains large particles and a variety of minerals absorbing over both spectral regions (e.g. iron
68 oxides, clays, quartz and calcium-rich species; Sokolik and Toon, 1999; Lafon et al., 2006; Di Biagio
69 et al., 2014a, b). Global and regional scale mapping of dust absorption remains limited and more infor-
70 mation is required (Samset et al., 2018).

71 Aerosol absorption is represented both by the imaginary part (k) of the complex refractive index ($m=n-$
72 ik) of its constituent material, and by the single scattering albedo (SSA, i.e., the ratio of the scattering
73 to extinction coefficient) of the particle population, as well as by the mass absorption efficiency (MAE,
74 units of $\text{m}^2 \text{g}^{-1}$), i.e., the aerosol absorption coefficient per unit mass concentration.

75 In the shortwave spectral range, absorption by dust accounts for up to ~10–20% of its total extinction.
76 Dust absorption is highest in the UV–VIS, and almost nil towards the near IR (Cattrall et al., 2003;
77 Redmond et al., 2010), due to the combined contribution of large particles in the size distribution and
78 the dust's mineralogy, notably the presence of iron oxides (Karickhoff and Bailey, 1973; Lafon et al.,
79 2006; Derimian et al., 2008; Moosmüller et al., 2012; Formenti et al., 2014a; 2014b; Engelbrecht et al.,
80 2016; Caponi et al., 2017). The mineralogy of airborne mineral dust varies according to that of the
81 parent soils (Nickovic et al., 2012; Journet et al., 2014). Consequently, dust aerosols of different origins
82 should be more or less absorbing in the SW, and have different imaginary spectral refractive index and

83 SSA. Field and laboratory measurements, including ground-based and space-borne remote sensing,
84 show that k varies at a regional scale by almost two orders of magnitude (0.0001–0.008 at 550 nm) with
85 corresponding SSAs between 0.80 and 0.99 at 550 nm (Volz 1972; Patterson et al., 1977; Shettle and
86 Fenn, 1979; Dubovik et al., 2002; Haywood et al., 2003; Sinyuk et al., 2003; Linke et al., 2006; Osborne
87 et al., 2008; Müller et al., 2009; Otto et al., 2009; Petzold et al., 2009; Schladitz et al., 2009; McConnell
88 et al., 2010; Formenti et al., 2011; Wagner et al., 2012; Ryder et al., 2013a; Engelbrecht et al., 2016;
89 Rocha-Lima et al., 2018). Albeit some variability being instrumental or analytical (differences in the
90 sampled size fraction or in the method used to retrieve optical parameters), geographic differences
91 persist when the same measurement approach and retrieval method are applied, e.g., in AERONET
92 inversions, supporting the dependence of dust k and SSA with its origin (Dubovik et al., 2002; Koven
93 and Fung, 2006; Su and Toon, 2011). In contrast, the real part (n) of the dust refractive index, mostly
94 related to particle scattering, is less variable, with values between 1.47–1.56 at 550 nm (e.g., Volz,
95 1972; Patterson et al., 1977; Balkanski et al., 2007; Petzold et al., 2009).

96 Differences in k or SSA caused by the spatial variability of the iron content may affect the sign of the
97 dust radiative effect (heating vs cooling) (Liao and Seinfeld, 1998; Claquin et al. 1999; Miller et al.,
98 2014), and its global and regional implications (Myhre and Stordal, 2001; Colarco et al., 2014; Das et
99 al., 2015; Jin et al., 2016; Bangalath and Stenchikov, 2016; Strong et al., 2018). The direct radiative
100 effect of dust has a strong impact on the Western African Monsoon (Yoshioka et al., 2007; Konaré et
101 al., 2008) and the Indian Summer Monsoon (Vinoj et al., 2014; Das et al., 2015; Jin et al., 2016). How-
102 ever, there is no consensus whether dust increases or decreases precipitation over these regions
103 (Solmon et al., 2008; Jin et al., 2016; Strong et al., 2018). As an example, Solmon et al. (2008) indicate
104 that dust reduces precipitation over most of the Sahelian region, but increases it over the Northern
105 Sahel–Southern Sahara. This pattern is, however, very sensitive to the dust absorbing properties, and
106 a decrease of few percent in dust absorption may even cancel out the increase of precipitation over the
107 Sahel. Similarly, Jin et al. (2016) show that by varying k from zero to 0.008 at 600 nm (i.e., the highest
108 value currently used in models) the dust effect on the Indian Summer Monsoon may shift from negative
109 (reduction of precipitation) to positive (increase of precipitation) values.

110 In spite of this sensitivity, present climate models adopt a globally-constant spectral complex refractive
111 index (and SSA) for dust, and hence still implicitly assume the same dust mineralogical composition at
112 the global scale. This is mainly due to the lack of a globally consistent dataset providing information of
113 the geographical variability of the dust scattering and absorption properties (e.g., Sunset et al., 2018).
114 Reference values for the refractive index are usually taken from Volz (1972), Patterson et al. (1977),
115 D’Almeida et al. (1991), Shettle and Fenn (1979), Sokolik et al. (1993), Sinyuk et al. (2003), or OPAC
116 (Optical Properties of Aerosols and Clouds, Hess et al., 1998; Koepke et al., 2015). A parameterization
117 of the spectrally-resolved dust refractive index as a function of the mineralogical composition of the
118 particles is desirable to replace the globally constant values in current climate models, in particular for
119 those models that started to incorporate the representation of dust mineralogy into their schemes
120 (Scanza et al., 2015; Perlwitz et al., 2015a, 2015b).

121 Improving our knowledge of the spectral SW refractive index of mineral dust and its relation to particle
122 composition (henceforth origin) is also key for the detection of dust aerosols in the atmosphere and the
123 quantification of its mass loading, and total or absorption spectral optical depth from active and passive
124 remote sensing (e.g., Ridley et al., 2016). As an example, the retrieval of the dust SSA and optical depth
125 over bright desert surfaces with the MODIS (Moderate Imaging Resolution Spectroradiometer) Deep
126 Blue algorithm (Hsu et al., 2004) applies the Critical Surface Reflectance Method (Kaufman, 1987) to
127 retrieve dust properties from measured Top of Atmosphere (TOA) spectral reflectance. This algorithm
128 depends critically on a priori information on the spectral refractive index (Kaufman et al., 2001; Yoshida
129 et al., 2013). Similarly, active remote sensing techniques (lidar, light detection and ranging) require the
130 knowledge of the extinction-to-backscatter ratio (the lidar ratio), which is also a strong function of the
131 complex index of refraction or SSA of the aerosol particles (e.g., Gasteiger et al., 2011; Shin et al.,
132 2018). Gasteiger et al. (2011) have shown in fact that a 5% change in the SSA at 532 nm can modify
133 by up to 20% the lidar ratio of dust, which means a 20% change in the estimated profile of the dust
134 extinction coefficient and retrieved optical depth from lidar measurements.

135 In this paper we address these issues by reporting of a new laboratory investigation of the shortwave
136 refractive index and SSA of dust from various source regions worldwide, in the framework of the RED-
137 DUST project (Di Biagio et al., 2017a; hereafter DB17; Caponi et al., 2017; hereafter C17). Dust optical
138 properties at discrete wavelengths between 370 and 950 nm are derived in conjunction with the particle
139 elemental and mineralogical composition, including total elemental iron and iron oxides. We investigate
140 the relationship of k and SSA to the iron content to provide a parameterization of the dust absorption
141 as a function of its mineralogy, which can be applied to climate models. The dependence of dust ab-
142 sorption on the particle coarse size fraction is also investigated to evaluate the change of dust absorp-
143 tion with atmospheric transport time.

144 **2. Experimental set-up and instrumentation**

145 As previously described in DB17 and C17, all experiments discussed here and were conducted in the
146 4.2 m³ stainless-steel CESAM chamber (French acronym for Experimental Multiphasic Atmospheric
147 Simulation Chamber) (Wang et al., 2011). Mineral dust aerosols were generated by mechanical shaking
148 of parent soils using about 15 g of soil sample (first sieved to <1000 μm and then dried at 100 $^{\circ}\text{C}$)
149 placed in a 1 L Büchner flask and shaken for about 30 min at 100 Hz by means of a sieve shaker
150 (Retsch AS200). The dust suspension in the flask was injected into the chamber by flushing with N₂ at
151 10 L min⁻¹ for about 10–15 min. After injection in the chamber, the largest fraction of the dust aerosol
152 (>1.5 μm diameter) remained in suspension for approximately 60 to 120 min thanks to a four-blade
153 stainless steel fan located at the bottom of the chamber, which also ensured homogeneous conditions
154 within the chamber volume. The submicron dust fraction, instead, remained constant with time during
155 the experiments (see Sect. 4.1.1). The evolution of the physico-chemical and optical properties of the
156 suspended dust was measured by different instruments connected to the chamber. The spectral particle
157 volume dry scattering (β_{sca}) and absorption (β_{abs}) coefficients were measured, respectively, by a 3-
158 wavelength nephelometer (TSI Inc. model 3563, operating at 450, 550, and 700 nm; 2 L min⁻¹ flow rate,
159 2-s time resolution) and a 7-wavelength aethalometer (Magee Sci. model AE31, operating at 370, 470,

160 520, 590, 660, 880 and 950 nm; 2 L min⁻¹ flow rate, 2-min time resolution). The size distribution of
161 aerosols was measured by means of a scanning mobility particle sizer (SMPS, TSI, DMA Model 3080,
162 CPC Model 3772; mobility diameter range 0.019–0.882 μm; 2.0/0.2 L min⁻¹ sheath–aerosol flow rates,
163 135-s time resolution), a WELAS optical particle counter (OPC) (PALAS, model 2000, white light source
164 between 0.35 and 0.70 μm; optical–equivalent diameter range 0.58–40.7 μm; 2 L min⁻¹ flow rate, 1–
165 min time resolution) and a SkyGrimm OPC (Grimm Inc., model 1.129, 0.655 μm operating wavelength;
166 optical–equivalent diameter range 0.25–32 μm; 1.2 L min⁻¹ flow rate, 6-s time resolution). Aerosol ele-
167 mental and mineralogical composition, including iron oxides, was derived by analysis of dust samples
168 collected on polycarbonate filters (47-mm diameter Nuclepore, Whatman, nominal pore size 0.4 μm)
169 mounted in a custom-made stainless-steel sample holder (operated at 6 L min⁻¹) for most of the dura-
170 tion of each experiment.

171 All instruments (size, SW optics, filters) sampled air from the chamber. To equalize the airflow extracted
172 by the different instruments, a particle-free N₂/O₂ mixture airflow was continuously injected into the
173 chamber. Inlets for all extractive measurements consisted of a stainless steel tube located inside
174 CESAM, and an external connection of silicone tubing (TSI Inc.) from the chamber to the instruments,
175 for a total length varying between 0.4 and 1.2 m. As detailed in DB17 and shown in Fig. S1 in the
176 supplement, the transmission efficiency due to aspiration and transmission in the sampling lines as a
177 function of particle diameter was estimated to calculate the effective dust fraction sensed by each in-
178 strument, taking into account the sampling flow rate, tubing diameter, tubing geometry, and particle
179 shape and density. For the nephelometer and the aethalometer, the length of the sampling line from
180 the intake point in the chamber to the instrument entrance was about 1.2 m, which resulted in a 50%
181 cutoff of the transmission efficiency at 3.9 μm particle geometric diameter and 100% cutoff at 10 μm.
182 For the filter sampling system, the length of the sampling line of about 0.5 m resulted in a 50% (100%)
183 cutoff at 6.5 μm (15 μm) particle geometric diameter (or 50% cutoff at 10.6 μm aerodynamic diameter
184 as indicated in C17, therefore compositional analyses refer to the PM_{10.6} size fraction). For the WELAS,
185 the only OPC considered for size distribution in the coarse fraction (see Sect. 2.2), the 50% (100%)
186 cutoff was reached for particles of 5 μm (8 μm) diameter.

187 All experiments were conducted at ambient temperature and relative humidity <2%. In addition to over-
188 night evacuation, the chamber was manually cleaned between experiments to avoid contaminations
189 from remaining dust. Background concentrations of aerosols in the chamber were less than 2.0 μg m⁻³
190 (that is 10² to 10⁵ times smaller than the concentration of dust aerosols in suspension in the chamber
191 during experiments)

192 A flowchart of the procedure used to treat and combine optical, size, and compositional data, and the
193 algorithm for SSA and complex refractive index retrieval is shown in Fig. 1. Full details of data treatment
194 for size distribution measurements and filter compositional data are provided in DB17 and C17, and in
195 the following we only mention the main points of interest for the present paper. Full details on the data
196 treatment of the SW optical data are provided in Sect. 2.1 and 3.

197 The optical and size datasets were acquired at different temporal resolutions and then averaged over
198 compatible 10-min intervals, whereas the compositional data represent the experiment integral. The

199 SSA and complex refractive index data were retrieved both at 10-min resolution and as experiment
200 averages to relate them to both size and compositional data. Table 1 summarizes the uncertainties on
201 the measured and derived parameters described in the following.

202 **2.1 SW optical measurements**

203 **2.1.1 Aerosol scattering coefficient**

204 The aerosol scattering coefficients (β_{sca}) at 450, 550, and 700 nm are measured by the nephelometer
205 at angles between 7° and 170° and need to be corrected for the restricted field-of-view of the instru-
206 ment (truncation correction) to retrieve β_{sca} at 0°–180°. The truncation correction factor (C_{trunc}), i.e., the
207 ratio of the β_{sca} at 0°–180° and 7°–170°, was estimated by Mie calculations for homogeneous spherical
208 particles using the size distribution measured simultaneously behind SW inlets (see Sect. 2.2). In the
209 calculations, the real part of the complex refractive index of dust was assumed to be wavelength-inde-
210 pendent and fixed at a value of 1.53, while the imaginary part was set to 0.003 at 450 and 550 nm and
211 to 0.001 at 700 nm, according to pre-existing information (Sinyuk et al., 2003; Schladitz et al., 2009;
212 Formenti et al., 2011; Rocha-Lima et al., 2018). For the different dust samples, C_{trunc} ranged between
213 1.2 and 1.7 and decreased with wavelength and the dust residence time in the chamber, following the
214 relative importance of the coarse component in the dust population. The uncertainty on C_{trunc} , calculated
215 by repeating the optical calculations by using the size distribution of dust within its error bars as input
216 to the optical code, is less than $\pm 5\%$ at all wavelengths. In order to assess the consistency of the derived
217 truncation correction, we made a sensitivity study in which we recalculated C_{trunc} by varying the refrac-
218 tive index used as input to the Mie calculations in the range of n and k values obtained in this study
219 (i.e., values at the 10% and 90% percentile as reported in Table 5 for the whole dataset, that is n
220 between 1.49 and 1.54 and k between 0.001 and 0.006 at 450, 550, and 700 nm). The results of this
221 sensitivity study indicate that, for fixed dust size distribution, the truncation correction C_{trunc} varies less
222 than 1% for n between 1.49 and 1.54, and $< 5\%$ for k between 0.001 and 0.006, and so that it is quite
223 insensitive to the exact assumed n and k values.

224 Once corrected for truncation, the spectral β_{sca} was extrapolated at the aethalometer wavelengths. With
225 this aim, the Scattering Ångström Exponents, $SAE_{450-550}$ and $SAE_{550-700}$, were calculated as the linear
226 fit of β_{sca} vs λ at 450–550 nm and 550–700 nm, respectively. The $SAE_{450-550}$ and $SAE_{550-700}$ coefficients
227 were used to extrapolate β_{sca} at wavelengths respectively lower and higher than 550 nm. Extrapolated
228 β_{sca} values were used to derive an average SAE of dust for the entire investigated spectral range.

229 **2.1.2 Aerosol absorption coefficient**

230 The aerosol absorption coefficient (β_{abs}) at 370, 470, 520, 590, 660, 880, and 950 nm was retrieved
231 from aethalometer measurements. The aethalometer measures the attenuation (ATT) through an aer-
232 osol-laden quartz filter, related to the spectral attenuation coefficient (β_{ATT}) as:

$$233 \quad \beta_{ATT}(\lambda) = \frac{\Delta ATT(\lambda) A}{\Delta t V} \quad (1)$$

234 where A is the area of the aerosol collection spot (0.5 ± 0.1) cm^2 and V the air sample flow rate (0.002
 235 $\text{m}^3 \text{min}^{-1}$). The slope $\frac{\Delta \text{ATT}(\lambda)}{\Delta t}$ is the linear fit of the measured attenuation as a function of time calcu-
 236 lated over 10-min intervals. The spectral attenuation coefficient was converted into an absorption co-
 237 efficient β_{abs} following the formula by Collaud Coen et al. (2010):

$$238 \quad \beta_{\text{abs}}(\lambda) = \frac{\beta_{\text{ATT}}(\lambda) - \alpha(\lambda)\beta_{\text{sca}}(\lambda)}{C_{\text{ref}}R(\lambda)} \quad (2)$$

239 The $\alpha(\lambda)\beta_{\text{sca}}(\lambda)$ term accounts for the fraction of the measured attenuation due to side and backward
 240 scattering and not to light absorption. The Collaud–Coen correction scheme has been recently shown
 241 to yield quite accurate values of the absorption coefficients and absorption Ångström exponents from
 242 aethalometer data (Saturno et al., 2017). The value of $\alpha(\lambda)$ was calculated with the formula by Arnott et
 243 al. (2005) and varied between 0.002 and 0.02 ($< \pm 1\%$ from formal error propagation on the Arnott for-
 244 mula), while $\beta_{\text{sca}}(\lambda)$ is the scattering coefficient from the nephelometer extrapolated to the aethalometer
 245 wavelengths. The C_{ref} term accounts for multiple scattering by the filter fibers, aerosol laden or not. Its
 246 spectral value, obtained by the linear extrapolation of C_{ref} at 450 and 660 nm estimated for mineral dust
 247 by Di Biagio et al. (2017b), varied between 4.30 at 370 nm and 3.32 at 950 nm. We assume for the
 248 extrapolated C_{ref} an uncertainty of $\pm 10\%$ as estimated in Di Biagio et al. (2017b). The correction factor,
 249 R , accounts for the decrease in the aethalometer sensitivity with the increase of the aerosol filter load-
 250 ing. The value of R depends on the absorptivity properties of the sampled aerosol and can be calculated
 251 as a function of the particle SSA. In this study, we calculated R by estimating a first-guess SSA^* as the
 252 ratio of the nephelometer-corrected β_{sca} and β_{ext} obtained as the sum of β_{sca} and the β_{abs} non-corrected
 253 for filter loading effect. The R was estimated by using the Collaud–Coen et al. (2010) formulation. For
 254 the range of estimated SSA^* (about 0.60 to 0.99), R varied between 0.5 and 1.0 ($\pm 1\text{--}10\%$).

255 The Absorption Ångström Exponent (AAE) was calculated as the power-law fit of β_{abs} versus λ .

256 Due to an instrumental problem, aethalometer data were not always available, with a typical 30-min
 257 interruption usually 10 to 30 minutes after the beginning of experiments.

258 **2.2 Size distribution**

259 The aerosol number size distribution was obtained from SMPS, WELAS and SkyGrimm measurements
 260 over different diameter ranges. The measured electrical mobility and optical equivalent diameters from
 261 the SMPS and the OPCs were first converted into geometrical diameters (D_g) as described in DB17
 262 and summarized in Table 1. The OPCs conversion assumes a dust complex refractive index that in our
 263 study was set in the range 1.47–1.53 for n and 0.001–0.005 for k for both the SkyGrimm and the WELAS
 264 (following DB17, for more details see Table 1). After conversion, the estimated D_g range was 0.01–0.50
 265 μm for the SMPS, 0.65–73.0 μm for the WELAS, and 0.29–68.2 μm for the SkyGrimm. Due to a cali-
 266 bration issue, data for the SkyGrimm in the range $D_g > 1 \mu\text{m}$ were discarded, so that the WELAS is the
 267 only instrument considered in the super-micron range. A very low counting efficiency was observed for
 268 the WELAS below 1 μm and data in this size range were also discarded.

269 The SMPS, WELAS, and SkyGrimm data were combined, as detailed in DB17, to obtain the full size
 270 distribution of the dust aerosols suspended in the CESAM chamber, $(dN/d\log D_g)_{CESAM}$, and the size
 271 distribution behind SW optical instruments inlets, $(dN/d\log D_g)_{SWoptics}$, after taking into account particle
 272 losses along sampling lines (see Supplementary material and Fig. S1). As previously discussed, due
 273 to the particle losses in the sampling line from the chamber to the nephelometer/aethalometer, the
 274 $(dN/d\log D_g)_{SWoptics}$ size distribution is cut at 10 microns, so no particles above this diameter reach the
 275 SW instruments.

276 The measured size distributions, $(dN/d\log D_g)_{CESAM}$ and $(dN/d\log D_g)_{SWoptics}$, were used to estimate the
 277 mass concentration of aerosols and their effective diameter (D_{eff}) in the CESAM chamber and behind
 278 the SW instrument inlets as:

$$279 \quad \text{Mass concentration} = \int \frac{\pi}{6} D_g^3 \frac{dN}{d\log D_g} \rho \cdot d\log D_g \quad (3)$$

$$280 \quad D_{eff} = \frac{\int D_g^3 \frac{dN}{d\log D_g} d\log D_g}{\int D_g^2 \frac{dN}{d\log D_g} d\log D_g} \quad (4)$$

281 The effective dust density ρ in Eq. (3) was set at 2.5 g cm^{-3} , a value that is approximately in the middle
 282 of the range of desert dust densities reported in the literature, i.e., $2.1\text{--}2.75 \text{ g cm}^{-3}$ (Maring et al., 2000;
 283 Iwasaka et al., 2003; Reid et al., 2003). The effective diameter was evaluated separately for the fine
 284 and coarse fractions of dust by integrating Eq. (4) for diameters $\leq 1 \text{ }\mu\text{m}$ ($D_{eff, fine}$) and $> 1 \text{ }\mu\text{m}$ ($D_{eff, coarse}$),
 285 respectively. For $D_{eff, coarse}$ the upper limit of the calculation is $10 \text{ }\mu\text{m}$ when calculated from
 286 $(dN/d\log D_g)_{SWoptics}$, i.e. measured behind the SW inlets.

287 The dust size distribution, $(dN/d\log D)_{SWoptics}$, measured at each 10-min time step for each sample was
 288 fitted with a sum of five lognormal functions to smooth data inhomogeneities linked to the different
 289 instrument's operating principles and artefacts. Fitting was performed using the Levenberg–Marquardt
 290 algorithm. For each mode, the parameters of the lognormal functions, i.e., the total number concentra-
 291 tion (N), the geometric median diameter ($D_{g,i}$), and the geometric standard deviation of the distribution
 292 (σ_i), were retrieved. The uncertainties in the retrieved parameters were estimated by repeating the fit
 293 using size data within their uncertainties. The resulting parameters of the fits at the peak of the injection
 294 in the chamber are reported in Table S1, and an example of size fitting is shown in Fig. S2.

295 The procedure described here to estimate $(dN/d\log D_g)_{CESAM}$ and $(dN/d\log D_g)_{SWoptics}$ implies that as-
 296 sumptions are made on the values of n and k to correct OPCs data, and this may introduce a circularity
 297 in the estimates of the refractive index of dust that use $(dN/d\log D_g)_{SWoptics}$ as input in optical calculations
 298 (see Sect. 3.2). In order to analyze the dependence of the results on this assumption, we made a
 299 sensitivity calculation by varying the values of n and k used for OPCs corrections within the range of
 300 values retrieved in this study (10% and 90% percentiles in Table 5, i.e., $1.49\text{--}1.54$ for n and 0.001--
 301 0.006 for k). We concluded that changing n and k in this range has a very low impact on the retrieved
 302 number size distribution behind the SW inlets $(dN/d\log D_g)_{SWoptics}$ compared to the original assumptions

303 made in our calculations (<5% changes in the retrieved size number distribution at the different diame-
304 ters between the original correction and the correction by varying n and k). This is due to the fact that
305 when changing D_g due to changes in the n and k in the OPCs correction, the loss function also modifies
306 to values corresponding to the new D_g . Given that the loss function increases/decreases for increas-
307 ing/decreasing D_g , the combined changes in D_g and the loss function compensate so that the net num-
308 ber concentration behind the SW inlets varies less than a few percent. These results therefore suggest
309 that the procedure to estimate the complex refractive index of dust is nearly independent of the assumed
310 OPC correction.

311 Other sources of uncertainties are linked to the spherical assumption to perform the optical to geomet-
312 rical diameter conversion (discussed in Sect. 3.3) as well as those due to Mie resonance oscillations of
313 the calculated scattering intensities. Concerning Mie resonances, a sensitivity study was performed
314 varying the size resolution of our calculations (high/low diameter resolution in the calculations to have
315 a better/worse reproduction of Mie resonance oscillations) and show that Mie resonances impact the
316 optical to geometrical correction by less than 1%.

317 **2.3 Dust elemental and mineralogical composition and iron content**

318 The elemental and mineralogical composition of the dust aerosols in the PM_{10.6} size fraction was esti-
319 mated by combining different techniques: X-ray diffraction (XRD, Panalytical model Empyrean diffrac-
320 tometer) to estimate the particles' mineralogical composition in terms of clays, quartz, calcite, dolomite,
321 gypsum, and feldspars; wavelength dispersive X-ray fluorescence (WD-XRF, Panalytical PW-2404
322 spectrometer) to determine the dust elemental composition (Na, Mg, Al, Si, P, K, Ca, Ti, Fe); and X-
323 ray absorption near-edge structure (XANES) to retrieve the content of iron oxides and their speciation
324 between hematite and goethite. The dust mass collected on Nuclepore filters during the experiments
325 varied between 0.3 and 6 mg m⁻³ as calculated from elemental concentrations according to Lide (1992).

326 Full details on the XRD, WD-XRF, and XANES measurements and data analysis are provided in DB17
327 and C17. In this study, we discuss the dust elemental iron mass concentration, MC_{Fe%}, i.e., the percent
328 mass of elemental iron with respect to the total dust mass concentration, and the iron oxides mass
329 concentration, MC_{Fe-ox%}, i.e., the percent mass fraction of iron oxides with respect to the total dust mass
330 concentration, estimated as the sum of goethite (MC_{Goet%}) and hematite (MC_{Hem%}) species.

331 **3. Strategy for data analysis**

332 **3.1 Calculation of the spectral extinction coefficient and SSA from scattering and absorption** 333 **coefficients**

334 The spectral scattering and absorption coefficients, $\beta_{sca}(\lambda)$ and $\beta_{abs}(\lambda)$, measured by the nephelometer
335 and the aethalometer were used to estimate 10-min averages of the spectral extinction coefficient, β_{ext}
336 (λ), at the 7- λ of the aethalometer between 370 and 950 nm as:

$$337 \quad \beta_{ext}(\lambda) = \beta_{abs}(\lambda) + \beta_{sca}(\lambda) \quad (5).$$

338 The Extinction Ångström Exponent (EAE) was calculated as the power-law fit of β_{ext} versus λ .

339 The spectral single scattering albedo of dust at 10-min resolution (SSA_{10-min}) was retrieved as:

340
$$SSA_{10\text{-min}}(\lambda) = \frac{\beta_{sca}(\lambda)}{\beta_{ext}(\lambda)} \quad (6).$$

341 The experiment-averaged SSA (λ) was calculated for each soil type based on the following formula
 342 (Moosmüller et al., 2012):

343
$$SSA(\lambda) = \left(1 + \frac{1}{m(\lambda)} \right)^{-1} \quad (7)$$

344 where $m(\lambda)$ represents the slope of the linear fit between the 10-min averages of $\beta_{sca}(\lambda)$ and $\beta_{abs}(\lambda)$
 345 measured along the whole duration of each experiment. An example of $\beta_{sca}(\lambda)$ versus $\beta_{abs}(\lambda)$ fitting to
 346 retrieve the spectral SSA is shown in Fig. S3 in the Supplement. The correlation coefficient R^2 of the
 347 $\beta_{sca}(\lambda)$ versus $\beta_{abs}(\lambda)$ fit usually ranges between 0.97 and 1 at all wavelengths. As will be discussed
 348 later in the paper, the single scattering albedo of dust depends on the particle coarse size fraction, and
 349 during our experiments $SSA_{10\text{-min}}$ was not derived continuously for the different samples due to the
 350 aethalometer measurement interruptions. The application of Eq. (7) avoids any bias in the calculated
 351 averaged SSA for different soils due to size effects. For two of the analyzed samples (Tunisia and
 352 Namib-2), however, the linear fitting procedure was not applicable due to the fact that, respectively,
 353 only two and one absorption measurements from the aethalometer were available just after the peak of
 354 the injection, with no data afterwards. Average SSA data for Tunisia were thus estimated as the mean
 355 of the two available $SSA_{10\text{-min}}$ data points, while the single $SSA_{10\text{-min}}$ measurement at the peak of the
 356 injection was reported for Namib-2. This difference in time sampling should be kept in mind when com-
 357 paring data for these two samples to the rest of the dataset.

358 3.2 Retrieval of the spectral complex refractive index

359 An optical calculation was performed to estimate the complex refractive index ($m=n-ik$) of dust aerosols
 360 based on optical and size data. The retrieval algorithm consisted in recalculating the spectral scattering
 361 $\beta_{sca}(\lambda)$ and absorption $\beta_{abs}(\lambda)$ coefficients measured at each 10-min interval by using the fitted
 362 $(dN/d\log D)_{SWoptics}$ size distribution as input and by varying the real and imaginary parts of the complex
 363 refractive index in the calculations until the best agreement between measurements and calculations
 364 was found. At each wavelength the root mean square deviation (RMSD) was calculated as:

365
$$RMSD(\lambda) = \sqrt{\left[\frac{\beta_{sca,measured}(\lambda) - \beta_{sca,calculated}(\lambda)(n,k)}{\beta_{sca,calculated}(\lambda)(n,k)} \right]^2 + \left[\frac{\beta_{abs,measured}(\lambda) - \beta_{abs,calculated}(\lambda)(n,k)}{\beta_{abs,calculated}(\lambda)(n,k)} \right]^2} \quad (8)$$

366 The RMSD was minimized at each wavelength to obtain $n-k$ pairs that most closely reproduce the
 367 measured scattering and absorption coefficients. Optical calculations were performed at the 7 wave-
 368 lengths of the aethalometer between 370 and 950 nm using Mie theory. In the calculations, the real part
 369 of the refractive index was varied in the range 1.40–1.60 at steps of 0.01, while the imaginary part was
 370 varied in the range 0.0001–0.050 at steps of 0.0001. For each sample, this resulted in 10500 compu-
 371 tations per wavelength and per 10-min time step. The uncertainty on the real and imaginary parts of
 372 the refractive index was estimated with a sensitivity study. For this purpose, the values of n and k were
 373 also obtained by using as input the observed $\beta_{sca}(\lambda)$, $\beta_{abs}(\lambda)$, and $(dN/d\log D)_{SWoptics}$, plus or minus one

374 standard deviation on their measurement. The deviations of the values of n and k retrieved in the sen-
375 sitivity study with respect to those obtained in the first inversions were assumed to correspond to the
376 one standard deviation uncertainty of 10-min retrieved values.

377 Experiment-averaged values of the spectral n and k were estimated as the average of single n and k
378 values retrieved at 10-min steps (indicated as n_{10-min} and k_{10-min}). In fact, differently from the SSA, the
379 refractive index did not seem to depend on the particle coarse size fraction (Sect. 4.5).

380 A control experiment was performed with submicron ammonium sulphate aerosols (see DB17 and sup-
381 plementary Fig. S4) with the aim of validating the proposed methodology to estimate the aerosol com-
382 plex refractive index for a non-absorbing aerosol type. For ammonium sulphate particles with a mono-
383 modal size distribution centered at 0.06 μm , as measured with the SMPS, the retrieved real part of the
384 refractive index was 1.56 (± 0.01) in the 450–700 nm wavelength range, as expected from literature
385 (Toon et al., 1976; Flores et al., 2009; Denjean et al., 2014).

386 **3.3 Assumptions on the retrieval of SSA and complex refractive index**

387 The approach used to retrieve the SSA and the complex refractive index of dust and the accuracy of
388 the results depend on the accuracy of the input data and the assumptions in the optical calculations.
389 We discuss here two points of the applied procedure, in part already mentioned in the previous para-
390 graphs.

391 1/ The size distribution from OPCs and also the scattering coefficient from the nephelometer used as
392 input to the n and k retrieval procedure and SSA calculation depend more or less directly on the dust
393 refractive index. These instruments need in fact to be corrected for instrumental artefacts and these
394 corrections require an a priori knowledge of the n and k , which in our approach were set to fixed values
395 (1.47–1.53 for n and 0.001–0.005 for k for OPCs optical to geometrical diameter conversion, and 1.53
396 for n and 0.001–0.003 for k for nephelometer truncation correction). This choice may in principle intro-
397 duce a certain degree of uncertainty and circularity into the derived n , k , and SSA for dust. Nonetheless,
398 we note that the range of refractive index values used to correct OPCs and nephelometer data falls in
399 the range of variability of the refractive index values obtained in this study (see Sect. 4.3), which sug-
400 gests that the values used for the corrections are appropriate. Additionally, as previously discussed,
401 both the size distribution ($dN/d\log D_g$)_{SWoptics} and the scattering coefficient are not very sensitive to the
402 assumptions about n and k used for the calculations (less than 5% changes in both the number size
403 distribution behind SW inlets and the scattering coefficient from changing n and k within the range of
404 estimated values in this study) which further demonstrates the robustness of the proposed approach.

405 2/ The retrieval procedure for n and k , as well as the calculations for OPCs optical-to-geometrical
406 diameter and the nephelometer truncation correction, simplifies the non-spherical heterogeneous dust
407 aerosols (e.g., Chou et al. 2008; Okada et al., 2011; Nousiainen and Kandler, 2015) into homogeneous
408 spherical particles that can be represented by Mie theory. In the present study, we decided not to use
409 a more advanced shape-representing theory for three main reasons. First, the spherical model has
410 been shown to produce only moderate errors when computing angular-integrated quantities
411 (Mishchenko et al., 1995; Otto et al., 2009; Sorribas et al., 2015) such as those we calculate in this

412 study to retrieve the OPC and truncation corrections and for n and k retrieval. For instance, Sorribas et
413 al. (2015) showed that using a spheroidal model has a limited effect on the truncation correction. These
414 authors estimated that using a spheroidal model permits to improve by 4 to 13% the agreement between
415 modelled and measured spectral scattering coefficient at 450–700 nm but only for supermicron parti-
416 cles. Conversely, for submicron dust the spherical approximation is better suited than the spheroidal
417 model to reproduce the scattering coefficients by the nephelometer. The study by Mogili et al. (2007)
418 also found an excellent agreement between measured shortwave extinction spectra and those calcu-
419 lated from Mie theory simulations for dust minerals, supporting the use of Mie theory for dust optical
420 modelling. On the other side, other studies point to the need of a non-spherical assumption to improve
421 the modelling of dust optical properties (e.g., Otto et al., 2009). Second, we used Mie theory for the
422 sake of comparison with the large majority of previous field and laboratory data published so far, which
423 had used calculations with the spherical approximation Third, the shape distribution and morphology of
424 the dust samples was not measured during experiments. Improper assumptions on the particle shape
425 and morphology may induce even larger errors than using Mie theory, in particular for super-micron
426 aerosols (Kalashnikova and Sokolik, 2004; Nousiainen and Kandler, 2015). It should be pointed out,
427 however, that dust is usually assumed to be spherical in global climate models (e.g., Myhre and Stordal,
428 2001; Balkanski et al., 2007; Jin et al., 2016), and different studies still show contradictory results on
429 the true impact of dust non-sphericity on radiative fluxes and heating rates from global model simula-
430 tions (Mishchenko et al., 1995; Yi et al., 2011; Räisänen et al., 2012; Colarco et al., 2014). On the other
431 hand, shape effects can be important for the retrieval of aerosol properties from remote sensing tech-
432 niques using spectral, angular, and polarized reflectance measurements (e.g., Feng et al., 2009). In
433 synthesis, accounting for shape effects is still controversial for dust modelling and also a complex issue
434 beyond the scope of this paper. Thus, while we acknowledge the potential uncertainties induced by
435 spherical assumptions in our study, we do not quantify here the overall impact of this assumption on
436 our results.

437

438 **4. Results**

439 Nineteen soil samples from different desert areas in Northern Africa, Sahel, Eastern Africa and the
440 Middle East, Central Asia, Eastern Asia, North America, South America, Southern Africa, and Australia
441 were selected for experiments from a collection of 137 soil samples from source areas worldwide. The
442 main information on the provenance of these soils is provided in Table 2. The nineteen selected soils,
443 the same as analyzed in DB17, represent the major dust source regions depicted in Ginoux et al. (2012).
444 Amongst the database of 137 samples from all the world regions that constitute significant dust emitters,
445 this range in mineralogical composition represents the largest variability in iron oxides contents that can
446 be found worldwide. This is illustrated in Fig. 2 where we represent the variability of hematite and goe-
447 thite content in the nineteen selected soils and compare it with the range of variability of the global
448 desert soils from the database of Journet et al. (2014).

449 **4.1 Physical and chemical properties of analysed dust samples**

450 **4.1.1 Dust mass concentration and size distribution**

451 Figure 3 shows a typical example of a time series of aerosol mass concentration and effective fine and
452 coarse diameters measured inside the CESAM chamber and behind the SW instruments inlets during
453 the experiments, as well as the corresponding β_{sca} and β_{abs} at 370 nm. The Figure shows the rapid
454 increase of the mass concentration within CESAM during dust injection in the chamber, and its subse-
455 quent decrease during the experiments due to both size-selective gravitational settling, occurring
456 mostly within the first 30 min of experiments, and dilution by sampling. The scattering and absorption
457 coefficients of dust decrease with time after injection in tandem with the decrease of the mass concen-
458 tration and the size-dependent depletion in the chamber. The dust mass concentration inside CESAM
459 at the peak of the injection is between 2 mg m⁻³ (Mali) and 310 mg m⁻³ (Bodélé) and falls to values
460 between 0.9 mg m⁻³ (Mali) and 20 mg m⁻³ (Bodélé) behind the SW instruments inlets. These values
461 are comparable to those measured close to sources during dust storms (Rajot et al., 2008; Kander et
462 al., 2009). After 2 hours, the dust mass concentration has decreased to values of 0.2 to 2.5 mg m⁻³
463 (inside CESAM) and of 0.1 to 1.9 mg m⁻³ (behind the SW inlets), as after medium- to long-range dust
464 transport in the real atmosphere (Weinzerl et al., 2011; Denjean et al., 2016b). This indicates that in a
465 2-hour experiment in CESAM it is possible to reproduce the temporal changes of the dust mass load
466 observed in the real atmosphere from emission to medium/long-range transport.

467 As the mass concentration, the effective diameter of the coarse fraction, $D_{eff,coarse}$, also rapidly de-
468 creases with time due the progressive deposition of the coarsest particles in the chamber. For the var-
469 ious soils, $D_{eff,coarse}$ varies in the range of 4–8 μm (peak of injection) to 3–4 μm (after 2 hours) inside the
470 CESAM chamber, and in the range of 3–4 μm (peak of injection) to 2–3 μm (after 2 hours) behind the
471 SW inlets. In contrast, $D_{eff,fine}$ remains quite constant during the experiments, with a value between 0.6
472 and 0.7 μm for all soils. The values of $D_{eff,coarse}$ obtained in this study inside the CESAM chamber are in
473 line with those measured close to African sources (4–12 μm , Rajot et al., 2008; Weinzerl et al., 2009;
474 Ryder et al., 2013a) and for dust transported across the Mediterranean (5–8 μm , Denjean et al., 2016a).
475 Conversely, the values of $D_{eff,coarse}$ behind the SW instruments inlets are mostly in agreement with those
476 reported for dust transported at Cape Verde and across the Atlantic ocean ($\sim 3 \mu\text{m}$, Maring et al., 2003;
477 Müller et al., 2011; Denjean et al., 2016b). Our values of $D_{eff,fine}$ are higher compared to values reported
478 by Denjean et al. (2016a) for dust aerosols transported over the Mediterranean (0.2 to 0.5 μm), reflect-
479 ing the fact that we analyse pure dust whereas these authors often encountered dust externally mixed
480 with pollution particles.

481 The comparison of $D_{eff,coarse}$ values suggests that while the size distribution in CESAM is mostly repre-
482 sentative of dust close to sources (see DB17), the size measured behind the SW instruments inlets is
483 mostly representative of transport conditions. Figure 4 illustrates this point by showing the volume size
484 distributions of the generated dust aerosols at the peak of injection seen by the SW optical instruments,
485 compared to the average size of dust measured in CESAM (DB17) and field observations close to
486 sources (e.g., Niger) and after long-range transport (Cape Verde, Suriname, Puerto Rico, and Barba-
487 dos). The size distribution of dust inside CESAM includes a coarse mode up to $\sim 50 \mu\text{m}$ and well repro-
488 duces field observations close to sources, as shown in comparison to the Niger case. Due to particle
489 losses along tubes, particles above 10 μm diameter are not seen by the SW instruments. The overall
490 shape of the dust size distribution sensed by the SW instruments is comparable to that measured after

491 atmospheric long-range transport, even if the fraction of particles above 3.9 μm diameter, which is at
492 the 50% cutoff of the transmission efficiency for the SW optical instruments, is significantly under-
493 represented compared to observations (i.e., Betzer et al., 1988; Formenti et al., 2001; Maring et al.,
494 2003; Ryder et al., 2013b, 2018; Jeong et al., 2014; Denjean et al., 2016b). It should be keep in mind
495 that often also field data are affected by inlet restrictions so that they cannot measure the whole coarse
496 dust fraction (see Table 1 in Ryder et al., 2018). The lowest cutoff for field data shown in Fig. 4 are for
497 the NAMMA and PRIDE datasets and correspond to upper size limits at 5 and 10 μm in diameter,
498 respectively. Being these values above our cutoff of 3.9 μm , it means that the comparison with our size
499 dataset is meaningful within the range of our measurements. To note that only the data from AER-D
500 did not suffer from significant inlet restrictions thus leading to the observation of giant dust particles up
501 to tens of microns in the Saharan Air Layer off the coasts of Western Africa.

502 **4.1.2 Iron and iron oxide dust content**

503 Elemental iron includes the iron in the form of iron oxides and hydroxides, i.e. hematite and goethite
504 (the so-called free iron, mostly controlling SW absorption) and the iron incorporated in the crystal struc-
505 ture of silicates and alluminosilicates (illite, smectite), which does not substantially contribute to SW
506 absorption (Karickhoff and Bailey, 1973; Lafon et al., 2004). The mass concentrations of these compo-
507 nents (total iron oxides, hematite, goethite, and total elemental iron) for the different analysed samples
508 are reported in Table 3. There is a considerable variability in the iron and iron oxide content for our
509 samples. Total iron in the dust samples is in the range from 2.4% (Namib-1) to 10.6% (Namib-2). Iron
510 oxides account for 11% to 62% of the iron mass (calculated following C17, not reported in Table 3),
511 whereas the percent of iron oxides to the total dust mass varies between 0.7% (Bodélé Depression)
512 and 5.8% (Niger). These data are in the range of values reported in the literature (Reid et al., 2003;
513 Scheuvens et al., 2013; Formenti et al., 2011, 2014a). For the samples from the Sahara and the Sahel,
514 goethite is the dominant iron oxide species, in agreement with Lafon et al. (2006) and Formenti et al.
515 (2014a; 2014b). Elsewhere, hematite dominates over goethite, as reported by some studies (Arimoto
516 et al., 2002; Shen et al., 2006; Lu et al., 2011).

517 **4.2 Spectral- and time-dependent dust extinction and absorption coefficients, complex refrac-** 518 **tive index, and SSA**

519 Figure 5 illustrates a typical spectral- and time-dependent set of measured optical properties. The
520 spectral extinction coefficient, absorption coefficient, SSA, and real and imaginary parts of the complex
521 refractive index obtained at 10-min resolution for the Morocco and Algeria samples are shown at the
522 peak of the dust injection in CESAM and 30 and 90 min after the peak. Figure 5 shows that absorption
523 decreases with wavelength, but not extinction. The SSA increases from 370 to 590 nm while it is almost
524 constant between 590 and 950 nm. The imaginary part of the refractive index decreases with λ following
525 the decrease of β_{abs} . The real part of the refractive index does not depend on wavelength.

526 The extinction and absorption coefficients decrease in absolute value with time, as already shown in
527 Fig. 3. Their spectral dependence remains quite constant with time, but varies from soil to soil. The
528 experiment-averaged absorption, scattering, and extinction Ångström exponents in the 370–950 nm

529 spectral range, representing the spectral variation of the absorption, scattering and extinction coeffi-
530 cients, vary between the values of 1.5 and 2.4 (AAE), -0.4 and 0.4 (SAE), and -0.2 and $+0.5$ (EAE)
531 for the different samples. These values are in line with those previously reported by Moosmüller et al.
532 (2012) and C17 for dust from various locations. The retrieved n and k also show negligible changes of
533 their spectral shape with time and their magnitude remains approximately constant. In contrast, the SSA
534 increases with time, in particular below 600 nm wavelength, and its spectral shape changes. This is
535 mostly due to the decrease of the coarse size fraction with residence time in the chamber, as will be
536 analysed in Sect. 4.5. Similarly to the absorption, scattering, and extinction coefficients, the spectral
537 shape of k and SSA is somewhat different between the various samples, with the sharpest spectral
538 variations observed for the most absorbing samples and a less pronounced spectral variation for the
539 less absorbing ones, as evident, for example, by comparing the SSA data for Morocco and Algeria in
540 Fig. 5.

541 **4.3 Spectral complex refractive index and SSA for the different source regions and comparison** 542 **to literature data**

543 Figures 6 and 7 show the experiment-averaged n , k , and SSA between 370 and 950 nm for the nine-
544 teen aerosol samples analyzed in this study. Data of n , k , and SSA and their uncertainties are reported
545 in Tables 4 and 5 for each sample together with the average values for each of the eight different source
546 regions and for the full dataset. Figures 6 and 7 show that there are significant differences, both in
547 magnitude and spectral shape, between the imaginary refractive index and SSA for the different sam-
548 ples. The highest values of k (0.0048 – 0.0088 at 370 nm and 0.0012 – 0.0021 at 950 nm) and lowest
549 values of SSA (0.70 – 0.75 at 370 nm and 0.95 – 0.97 at 950 nm) are obtained for the Niger, Mali, Namib-
550 2 and Australia samples, which also show the highest values of both the iron oxide content between
551 3.6% and 5.8% and hematite content between 2.0% and 4.8% . The lowest values (k is 0.0011 – 0.0012
552 at 370 and 0.0003 – 0.0004 at 950 nm, and SSA is in the range 0.91 – 0.96 at 370 nm and 0.97 – 0.99 at
553 950 nm) are obtained for the Bodélé, Namib-1, and Arizona samples, which have iron oxide contents
554 between 0.7% and 1.5% . Both k and SSA vary from region to region, with the largest absorptions (high-
555 est k , lowest SSA) for the Sahel and Australia and the lowest absorption (lowest k , highest SSA) in
556 North and South America and the Middle East; k and SSA values also vary within the same region, as
557 illustrated for the Sahelian and Southern African samples. The real part of the refractive index, on the
558 other hand, is not only almost wavelength-independent, as anticipated, but also relatively invariant from
559 sample to sample. Its average over the 370–950 nm spectral range is between 1.48 (Gobi) and 1.55
560 (Ethiopia and Namib-2).

561 The full envelope of n , k , and SSA obtained for the entire set of analysed samples is shown in Fig. 8.
562 The real refractive index is relatively invariant, while the spectral k varies by up to an order of magnitude
563 (0.001 – 0.009 at 370 nm and 0.0003 – 0.002 at 950 nm). The SSA changes accordingly for the different
564 dust samples at the different wavelengths (30% change at 370 nm corresponding to values between
565 0.70 – 0.96 and 4% change at 950 nm for values within 0.95 – 0.99). The population mean is 1.52 for n
566 (as spectral average) and varies in the range 0.0033 – 0.0009 for k and 0.85 – 0.98 for the SSA between
567 370 and 950 nm (0.0016 and 0.94 as spectral averages for k and SSA) (Fig. 8 and Tables 4 and 5).

568 The comparison between the full envelope of n , k , and SSA in this study with literature data is also
569 shown in Fig. 8. Literature values considered for comparison include estimates from ground-based,
570 aircraft, and satellite observations, laboratory studies, AERONET inversions, and estimates from mixing
571 rules based on the dust mineralogical composition. Given that the sample selection in our experiments
572 fully envelopes the global variability of mineralogy of natural dust, we could expect that our dataset
573 would also fully envelope the global-scale variability of the dust absorption and scattering properties in
574 the SW. When comparing with available literature data we found that our n and SSA datasets very well
575 encompass the range of values indicated in the literature, with only a few outlier points. In contrast, for
576 the imaginary refractive index the reported range of variability from the literature is significantly larger
577 than that found in our study, with our range of k being mostly at the lower bound of previous results.
578 Nonetheless, our range of k values fully envelopes the ensemble of remote sensing and field campaign
579 data on airborne dust from the previous literature reported in Fig. 8a. The global average spectral values
580 for k in our study (thick black line) perfectly match the Dubovik et al. (2002) dataset from a synthesis of
581 AERONET observations from various locations worldwide. Likewise, our k average is also very close
582 to the dataset by Balkanski et al. (2007), estimated from mineralogical composition assuming 1.5% (by
583 volume) of hematite in dust, a value shown to allow a reconciliation of climate modelling and satellite
584 observations of the dust direct SW radiative effect. By comparison, the average dust hematite content
585 for the ensemble of our analysed samples is 1.8% (in mass), close to the 1.5% value proposed by
586 Balkanski et al. (2007).

587 Looking at Fig. 8, the datasets that show the largest values, which also fall outside our estimated range
588 of k over the entire considered wavelength range are the ones by: (i) Volz (1972), Patterson et al. (1977)
589 and Hess et al. (1998; i.e., the OPAC 3.1 version database, which is the same k dataset used in the
590 new OPAC 4.0 version, Koepke et al., 2015) showing larger values than our dataset over the entire
591 considered wavelength range. These datasets are amongst the most commonly used references for
592 the dust imaginary refractive index in many climate models; and (ii) the dataset by Wagner et al. (2012)
593 obtained from laboratory chamber experiments, deviating especially below 600 nm wavelength from
594 our range of k . The reasons for these discrepancies in the k values are difficult to assess, since they
595 could be related to both instrumental and analytical aspects. In the studies by Volz (1972) and Patterson
596 et al. (1977), for instance, the complex refractive index was obtained by transmittance and diffuse re-
597 flectance on pellet samples, a technique that requires the dust to be pressed in a matrix of non-absorb-
598 ing material. In this case a discrepancy arises from the different optical behaviour between dust com-
599 pressed in a pellet and the airborne particles. Moreover, Volz (1972) and Patterson et al. (1977) analyse
600 dust aerosols collected after mid- to long-range transport, thus after the dust has possibly been mixed
601 with absorbing species.

602 For the case of Wagner et al. (2012) the imaginary refractive index was retrieved from laboratory cham-
603 ber experiments on suspended dust, as in our study. Nonetheless, their approach differs in various
604 aspects from the one applied here and this can lead to the observed differences in the retrieved k . First,
605 the aerosol generation technique is different between the two works and this possibly leads to particles
606 with different physico-chemical features compared to our study. In Wagner et al. (2012) the dust aerosol
607 was generated by a rotating brush disperser using only the 20–75 μm sieved fraction of the soils. This

608 system acts to disaggregate the finest particles of the soil by passing it through a nozzle. Then the
609 largest aerosol grains were removed by a cyclone system (50% cutoff at 1.2 μm aerodynamic diameter),
610 so that only the submicron size fraction was measured. We show in Sect. 4.5 that k is independent of
611 size for the range of investigated effective coarse diameters between 2 and 4 μm , but the range of sizes
612 analysed in Wagner et al. (2012) is significantly lower than in our study and a size–effect cannot be
613 excluded. In fact, the relationship between dust absorption and iron content may vary depending on the
614 considered size fraction (see C17) due to the fact that iron bearing minerals are more concentrated in
615 the clay fraction (<2.0 μm) of the dust (Kandler et al., 2009). Moreover, generating dust in a different
616 way may lead to differences in the chemical and mineralogical size–dependent composition of the sam-
617 ple, therefore contributing to the observed differences. The impact of this is however difficult to evaluate.
618 Another difference concerns the choice of the optical theory to retrieve k (T–matrix in Wagner et al.
619 instead of Mie theory as used in our work). This can contribute to the observed differences, even in a
620 limited way (Mogili et al., 2007; Sorribas et al., 2015). Third, in their retrieval Wagner et al. fixed the real
621 refractive index to a wavelength–independent value of 1.53 (as done in several other field and labora-
622 tory studies in Fig. 8) and this assumption can bias high/low the retrieved k if the actual n is higher/lower
623 than the assumed 1.53 value. So, in summary, while multiple factors could contribute to the discrepancy
624 it remains however difficult to assess which source of discrepancy is dominant.

625 **4.4 Imaginary refractive index and SSA versus iron and iron oxide content**

626 The sample–to–sample variability of the imaginary part of the refractive index k and the SSA observed
627 in Fig. 6 and 7 is related to the dust composition by investigating the dependence on the particle iron
628 content. In Fig. 9 we show the experiment–averaged k and SSA at 370, 520, and 950 nm versus the
629 mass concentration of iron oxides (hematite+goethite, $\text{MC}_{\text{Fe-ox}\%}$), hematite ($\text{MC}_{\text{Hem}\%}$), goethite
630 ($\text{MC}_{\text{Goeth}\%}$), and total elemental iron ($\text{MC}_{\text{Fe}\%}$) measured for the different dust samples in this study. The
631 data are linearly fitted to relate k and SSA to $\text{MC}_{\text{Fe-ox}\%}$, $\text{MC}_{\text{Hem}\%}$, $\text{MC}_{\text{Goeth}\%}$, and $\text{MC}_{\text{Fe}\%}$. The results of
632 the fits at all wavelengths between 370 and 950 nm are reported in Table 6, together with the statistical
633 indicators of the goodness of fit (correlation coefficient, R^2 , and reduced chi square, χ^2_{red} , i.e., the ob-
634 tained chi square divided by the number of degrees of freedom). There is an excellent correlation be-
635 tween both k and SSA and $\text{MC}_{\text{Fe-ox}\%}$ at the different wavelengths ($R^2 > 0.75$). A weaker correlation is
636 found when relating k and SSA to $\text{MC}_{\text{Hem}\%}$ and $\text{MC}_{\text{Fe}\%}$ (R^2 between 0.40 and 0.74 for k and between
637 0.49 and 0.78 for the SSA), and $\text{MC}_{\text{Goeth}\%}$ (R^2 between 0.17 and 0.62). The better correlation of k and
638 SSA to $\text{MC}_{\text{Fe-ox}\%}$ compared to $\text{MC}_{\text{Fe}\%}$ is expected since dust optical properties in the visible wavelengths
639 are mostly sensitive to the fraction of iron oxides, rather than to iron incorporated into the crystal struc-
640 ture of silicates (Karickhoff and Bailey, 1973; Lafon et al., 2006; Moosmüller et al., 2012; Klaver et al.,
641 2011; Engelbrecht et al., 2016; C17). The quantities that most robustly satisfy a linear relationship are
642 k and $\text{MC}_{\text{Fe-ox}\%}$, as indicated by the reduced chi square χ^2_{red} that is around 1 at all different wavelengths.
643 The χ^2_{red} increases to values also larger than 2 in the other cases, indicating the poorer robustness of
644 the fit in these cases.

645 We also investigated the dependence of the spectral k and SSA on the mass concentration of other
646 minerals, such as clays, calcite, quartz, and feldspars, and also on the mass concentration of different

647 elements. We found that there is no statistically significant correlation between k or SSA and the mass
648 concentration of any of these compounds (not shown), with R^2 values between 0.002 and 0.46 at the
649 different wavelengths for all cases.

650 These results therefore clearly show that iron, particularly in the form of iron oxides (hematite + goe-
651 thite), is the main driver of dust shortwave absorption. Measuring only the hematite mass fraction to
652 estimate the dust absorption, as it is sometimes done, is therefore not sufficient.

653 **4.5 Imaginary refractive index and SSA versus dust coarse size fraction**

654 The dependence of the spectral k and SSA on the dust coarse fraction is investigated by relating it to
655 the $D_{eff,coarse}$ calculated from the size distribution data behind the SW instruments inlets. The k_{10-min} and
656 SSA_{10-min} at 370, 520, and 950 nm versus $D_{eff,coarse}$ are shown in Fig. 10 for all experimental data, which
657 we separated into three classes based on their iron oxide content ($MC_{Fe-ox\%} \leq 1.5\%$, $1.5\% < MC_{Fe-ox\%}$
658 $< 3\%$, $MC_{Fe-ox\%} \geq 3\%$). Figure 10 shows that even if the correlation is not very strong ($R^2 < 0.54$), there
659 is a clearly decreasing tendency for the SSA_{10-min} with increasing $D_{eff,coarse}$, particularly at 370 and 520
660 nm for strongly absorbing samples with iron oxide content larger than 3%. The SSA_{10-min} is mostly
661 independent of changes of $D_{eff,coarse}$ at 950 nm. Conversely, k_{10-min} has a very poor correlation with
662 $D_{eff,coarse}$ ($R^2 < 0.35$) and thus does not depend on size. Similar results were also obtained for the real
663 part (not shown).

664 These results confirm previous observations (Sokolik and Toon, 1999; McConnell et al., 2008, 2010;
665 Ryder et al., 2013a; 2013b) that the refractive index is independent of size. This suggests that size-
666 dependent mineralogical composition is not sufficient to affect k (in the limit of our measurement and
667 retrieval procedure precision). It is worth mentioning that only few past studies evidenced a dependence
668 of k on the size distribution of the dust aerosols (i.e., Kandler et al., 2009, 2011; Otto et al., 2009) maybe
669 because the refractive index was retrieved in these studies from mixing rules based on the estimated
670 size-dependent mineralogical composition.

671 Differently from k , the SSA increases as the coarse dust size fraction decreases. This is due to the fact
672 that absorption efficiency for a single particle (Q_{abs}) increases with particle diameter while the scattering
673 efficiency (Q_{sca}) decreases. Ryder et al. (2013a) also showed that the dependence of SSA on size is
674 linear, but important only when the coarse fraction is high (if particles larger than about 3 μm in diameter
675 are present), otherwise the SSA depends mainly on composition, also in agreement with more recent
676 field observations by Ryder et al. (2018).

677 **5. Summary**

678 In this paper we presented new measurements of the spectral SW complex refractive index ($m=n-ik$)
679 and single scattering albedo (SSA) for nineteen mineral dust aerosols generated in the laboratory from
680 natural soil samples from major desert dust source areas in northern Africa, the Sahel, Middle East,
681 eastern Asia, North and South America, southern Africa, and Australia, and selected to represent the
682 heterogeneity of the dust composition at the global scale, in particular the range of iron oxide concen-
683 trations. The envelope of refractive indices and SSA data obtained in this study can thus be taken as
684 representative of the variability of the global dust aerosol.

685 Experiments described here were conducted in the 4.2 m³ CESAM chamber, a dynamic environment
686 where dust aerosols are generated and maintained in suspension for several hours while monitoring
687 the evolution of their physical, chemical, and optical properties. The generated dust aerosols are char-
688 acterized by a realistic size distribution, including both the sub-micron and the super-micron fraction,
689 and they have an atmospherically representative mass concentration and composition, including iron
690 oxides and elemental iron content.

691 Some other laboratory studies have been performed in the past to investigate the shortwave SSA of
692 dust from different sources worldwide and its dependence on composition (Linke et al., 2006; Moosmül-
693 ler et al., 2012; Engelbrecht et al., 2016). Conversely, for the refractive index there exists to our
694 knowledge only one other chamber study (Wagner et al., 2012), that retrieved the imaginary part k
695 between 305 and 955 nm for dust aerosols from a limited number of source areas in Africa (Burkina
696 Faso, Egypt and Morocco). As a matter of fact, our work provides the first consistent simulation chamber
697 study of the complex refractive index of global dust.

698 The results of the present study can be summarized as follows:

- 699 1. The spectral k and SSA retrieved in this study vary from sample to sample within the same region
700 but also from a region to another. For k , values vary between 0.0011–0.0088 at 370 nm, 0.0006 to
701 0.0048 at 520 nm, and 0.0003–0.002 at 950 nm. For SSA, values vary from 0.70 to 0.96 at 370 nm,
702 0.85 to 0.98 at 520 nm, and from 0.95 to 0.99 at 950 nm. In contrast, n is wavelength-independent
703 and almost uniform for the different sources, with values between 1.48 and 1.55. Values for n and
704 SSA fall within the range of published literature estimates, while for k we obtain a much narrower
705 range of variability than the ensemble of literature results, as illustrated in Fig. 8. In particular, we
706 found lower values of k compared to most of the literature values currently used in climate models,
707 such as Volz et al. (1972), Patterson et al. (1977), and the OPAC database (Hess et al., 1998;
708 Koepke et al., 2015). In their study, Miller et al. (2014) state that the values of Dubovik et al. (2002)
709 from AERONET, Patterson et al. (1977) for far-travelled dust, and OPAC probably bracket the
710 global solar absorption by dust. In contrast, our results indicate that dust absorption is lower than
711 previously thought, and its average is close to the values reported by Dubovik et al. (2002) from
712 AERONET observations and Balkanski et al. (2007) for a dust with a 1.5% volume fraction of hem-
713 atite. Our range of variability of an order of magnitude for k and between 4% and 30% for the
714 spectral SSA is actually large enough to change the sign of the global dust direct effect at the TOA
715 (Miller et al., 2004), as well as its regional implications (e.g., Solmon et al., 2008; Jin et al., 2016),
716 and has to be taken into account in climate modelling.
- 717 2. The documented changes in k and SSA also impact remote sensing retrievals. To give an example,
718 following Gasteiger et al. (2011), our observed variability of about 10% for the SSA at 532 nm would
719 translate to about 40% variability in the retrieved extinction profiles and optical depths from lidar
720 observations for dust from varying sources.
- 721 3. The sample-to-sample variability observed in this study is mostly related to the iron oxide and
722 elemental iron content in dust. At each investigated wavelength the magnitude of k and SSA is

723 linearly correlated to the mass concentration of total iron oxides, hematite, goethite, and total ele-
724 mental iron. Small variations of these compounds translate into large variations of k and SSA.

725 4. We also investigated the dependence of k and SSA on the size distribution of dust. While k is
726 independent of size (suggesting that a constant value can be used along transport), below 600 nm
727 the SSA linearly decreases for increasing $D_{eff,coarse}$ for strongly absorbing samples with more than
728 3% iron oxide content. The investigated range of $D_{eff,coarse}$ is within about 2 and 4 μm , and thus
729 comparable to values obtained along a transport path over the Atlantic Ocean for dust during about
730 2 to 6 days following emission (Denjean et al., 2016a).

731 5. The observations of points 3 and 4 suggest that while it is sufficient to know the content of iron
732 oxide (or elemental iron) in dust to predict its spectral k , which means that only one tracer is needed
733 in models to parametrize its regional and global variability, for the spectral SSA both composition
734 and size distribution are required.

735 **6. Concluding remarks**

737 Based on our results, we recommend that dust simulations, as well as remote sensing retrievals, use
738 source-dependent values of the spectral SW refractive index and SSA instead of generic values. We
739 propose, as a first step, a set of regionally-averaged n , k , and SSA values to represent dust from each
740 of the eight regions analysed here as well as a global average value from the ensemble of our data
741 (Tables 4 and 5). Furthermore, the relationships found between k and SSA and the iron oxides or ele-
742 mental iron content in dust open the perspective to establish predictive rules to estimate the spectrally-
743 resolved SW absorption of dust based on composition. We recommend the use of iron oxide content
744 rather than iron content as it is better correlated with k and SSA. The relationship found in this study,
745 nonetheless, refer to the bulk composition of the dust aerosols and to a size range typical of 2 to 6 days
746 of transport in the atmosphere. As demonstrated in C17 for the mass extinction efficiency, the relation-
747 ships linking the dust absorption to iron content vary as a function of the analysed size fraction due to
748 the fact that iron bearing minerals are more concentrated in the clay fraction ($<2.0 \mu\text{m}$) than in the
749 coarsest fraction of the dust (Kandler et al., 2009; C17). Further investigation should be therefore ad-
750 dressed to evaluate the dependence of the spectral k and SSA versus iron content as a function of the
751 size distribution of the particles, in particular extending to a wider range of $D_{eff,coarse}$ compared to the
752 one investigated in the present study. This will allow to determine if the k and SSA versus iron relation-
753 ships change or not in different phases of the aerosol lifetime, so if it is valid close to source areas
754 (when the coarsest fraction is dominant, i.e. $D_{eff,coarse}$ up to 15 μm , Ryder et al. (2013b)), and in long-
755 range transport conditions (when most of the coarse particle fraction above few μm has settled out (i.e.,
756 $D_{eff,coarse}$ of 2–3 μm or lower, Denjean et al. (2016b)).

757 We point out, however, that the use of mineralogy to estimate k and SSA based on linear relationships,
758 as obtained in our study, requires that the model-predicted dust composition accurately reflects that of
759 the natural atmospheric aerosols. To this aim, realistic soil mineralogy databases and accurate model-
760 ling of the soil to aerosol size fractionation need to be developed in model schemes. In this sense we
761 mention the EMIT project (Earth Surface Mineral Dust Source Investigation) as a potential near-future
762 source of high resolution surface mineralogy data for arid and semi-arid regions based on imaging

763 spectroscopy satellite data (Green et al., 2018). Also, a realistic representation of the size distribution,
764 in particular the coarse mode fraction of dust and its retention during atmospheric transport, should be
765 provided in models given its importance in affecting the SSA, as shown in this study and previously
766 reported in other papers (Ryder et al., 2013a, 2013b, 2018; Kok et al., 2017).

767 Our study focuses on the dust spectral optical properties between 370 and 950 nm. Further work is
768 required to extend the range of spectral refractive index and SSA data to wavelengths lower than 370
769 nm or higher than 950 nm given that these data are often required in Global Circulation Models and
770 Numerical Weather Prediction models.

771 We do not provide any quantification of the uncertainty associated with the assumption of spherical
772 particles in our study, even if we acknowledge the potential role of non-sphericity in affecting our data
773 treatment and results. Additional work is foreseen to better investigate the shape of our generated dust
774 and the impact of non-sphericity on retrieved spectral refractive indices and SSA.

775 Finally, this study had the objective to investigate the variability of the dust SW optical properties at the
776 global scale linked to the global variability of the dust composition. It is noteworthy that observations
777 over Southern Africa and the Sahel from the present study indicate that the k and SSA variability over
778 these regions is comparable to the one obtained for the global scale. For other regions, such as North
779 America and Australia, only one sample was analyzed, with no information on the regional-scale vari-
780 ability of k and SSA. Additionally, for some of the analyzed areas, such as the Bodélé depression, even
781 local scale variability (on the order of few km) may be of relevance, given the documented local scale
782 changes of the particles' mineralogy and iron content (Bristow et al., 2010). More efforts should be
783 therefore devoted to better characterize the variability of dust spectral optical properties at the regional
784 and sub-regional scale with the aim of better assessing the dust impact on the climate of different areas
785 of the world.

786

787 **Data availability**

788 Complex refractive index and single scattering albedo data for the different analyzed samples are pro-
789 vided in Tables 4 and 5 and will be compiled together with aerosol properties from other studies within
790 the Library of Advanced Data Products (LADP) of the EUROCHAMP datacenter ([https://data.euro-
792 champ.org](https://data.euro-
791 champ.org)). The CESAM data used in this study are immediately available upon request to the contact
793 author and will also soon be made available through the Database of Atmospheric Simulation Chamber
794 Studies (DASCS) of the EUROCHAMP datacenter ([https://data.eurochamp.org /](https://data.eurochamp.org/)).

794

795 **Code availability**

796 The following IDL routines were used in the analysis: mpfitexy.pro (available at [https://github.com/wil-
798 liamsmj/mpfitexy](https://github.com/wil-
797 liamsmj/mpfitexy)) was used to linearly fit data taking into account uncertainties on both x and y ; mie_sin-
799 gle.pro (available at [http://www.atm.ox.ac.uk/code/mie/mie_ single.html](http://www.atm.ox.ac.uk/code/mie/mie_single.html)) was used for optical calcula-
800 tions using Mie theory; mpcurvefit.pro (available at <http://cow.physics.wisc.edu/~craigm/idl/idl.html>) was
used for size lognormal fitting.

801

802 **Author contributions**

803 C. Di Biagio, P. Formenti, Y. Balkanski, and J. F. Doussin designed the experiments and discussed the
804 results. C. Di Biagio performed the experiments and performed the full data analysis with contributions
805 by P. Formenti, L. Caponi, M. Cazaunau, E. Pangui, and J.F. Doussin. The soil samples used for ex-
806 periments were collected by M. O. Andreae, K. Kandler, T. Saeed, S. Piketh, D. Seibert, and E. Wil-
807 liams. E. Journet participated to the selection of the soil samples for experiments. S. Nowak performed
808 the XRD measurements. C. Di Biagio and P. Formenti wrote the manuscript with comments from all
809 co–authors.

810

811 **Acknowledgements**

812 The RED–DUST project was supported by the French national programme LEFE/INSU and by the
813 OSU–EFLUVE (Observatoire des Sciences de l’Univers–Enveloppes Fluides de la Ville à l’Exobiologie)
814 through dedicated research funding. The authors acknowledge the CNRS–INSU for supporting the
815 CESAM chamber as national facility and the AERIS datacenter (www.aeris-data.fr) for distributing and
816 curing the data produced by the CESAM chamber through the hosting of the EUROCHAMP datacenter.
817 This work has received funding from the European Union’s Horizon 2020 research and innovation pro-
818 gramme through the EUROCHAMP–2020 Infrastructure Activity under grant agreement no. 730997. C.
819 Di Biagio was supported by the CNRS via the Labex L–IPSL, funded by the ANR (grant no. ANR–10–
820 LABX–0018). K. Kandler is funded by the Deutsche Forschungsgemeinschaft (DFG, German Research
821 Foundation) – 264907654; 416816480 (KA 2280). Field sampling in Saudi Arabia was supported by a
822 grant from King Saud University. The authors thank the LISA staff, who participated in the collection of
823 the soil samples from Tunisia, Niger, Atacama, Patagonia, and the Gobi desert used in this study, and
824 S. Caquineau (LOCEAN), S. Chevallier (LISA) and G. Landrot (synchrotron SOLEIL), for their contri-
825 bution in the XRD, WD–XRF and XANES analyses. C. Di Biagio thanks P. Stegmann for providing
826 corrected refractive index data shown in Fig. 8. The authors wish also to acknowledge C. Ryder and C.
827 Pérez Garcia Pando for providing valuable comments that helped to increase the readability and quality
828 of the paper.

829

830 **Competing interests**

831 The authors declare that they have no conflict of interest.

832

833

834 **References**

835

- 836 Anderson, T. L. and Ogren, J. A.: Determining aerosol radiative properties using the TSI 3563 integrating nephe-
837 lometer, *Aerosol Sci. Technol.*, 29, 57–69, 1998.
- 838 Arimoto, R., Balsam, W., and Schloesslin, C.: Visible spectroscopy of aerosol particles collected on filters: iron–
839 oxide minerals, *Atmos. Environ.*, 36, 89–96, 2002.

840 Arnott, W., Hamasha, K., Moosmüller, H., Sheridan, P. J., and Ogren, J. A.: Towards aerosol light-absorption
841 measurements with a 7-wavelength aethalometer: Evaluation with a photoacoustic instrument and 3-wave-
842 length nephelometer, *Aerosol Sci. Tech.*, 39(1), 17–29, 2005.

843 Balkanski, Y., Schulz, M., Claquin, T., and Guibert, S.: Reevaluation of Mineral aerosol radiative forcings suggests
844 a better agreement with satellite and AERONET data, *Atmos. Chem. Phys.*, 7, 81–95, doi:10.5194/acp-7-81-
845 2007, 2007.

846 Bangalath, H.K. and Stenchikov, G.: Sensitivity of the Middle East–North African Tropical Rainbelt to Dust
847 Shortwave Absorption: A High-Resolution AGCM Experiment. *J. Climate*, 29, 7103–7126,
848 <https://doi.org/10.1175/JCLI-D-15-0827.1>, 2016.

849 Betzer, P., Carder, K., Duce, R., & Merrill, J.: Long range transport of giant mineral aerosol particles. *Nature*, 336,
850 568–571, 1988.

851 Boucher, O., et al., Clouds and Aerosols. Stocker, T., & Qin, D. (eds), *Climate Change 2013: The Physical Science*
852 *Basis. Contribution of Working Group I to the Fifth Assessment Report of the Intergovernmental Panel on Cli-*
853 *mate Change.* Cambridge Univ. Press, Cambridge, United Kingdom and New York, NY, USA, 2013.

854 Bretl, S., P. Reutter, C. C. Raible, S. Ferrachat, C. Schnadt Poberaj, L. E. Revell, and U. Lohmann: The influence
855 of absorbed solar radiation by Saharan dust on hurricane genesis, *J. Geophys. Res. Atmos.*, 120,
856 doi:10.1002/2014JD022441, 2015.

857 Bristow, C. S., Hudson-Edwards, K. A., and Chappell, A.: Fertilizing the Amazon and equatorial Atlantic with West
858 African dust, *Geophys. Res. Lett.*, 37, L14807, doi:10.1029/2010GL043486, 2010.

859 Caponi, L., Formenti, P., Massabó, D., Di Biagio, C., Cazaunau, M., Pangui, E., Chevallier, S., Landrot, G., An-
860 dreae, M. O., Kandler, K., Piketh, S., Saeed, T., Seibert, D., Williams, E., Balkanski, Y., Prati, P., and Doussin,
861 J.-F.: Spectral- and size-resolved mass absorption efficiency of mineral dust aerosols in the shortwave spec-
862 trum: a simulation chamber study, *Atmos. Chem. Phys.*, 17, 7175–7191, [https://doi.org/10.5194/acp-17-7175-](https://doi.org/10.5194/acp-17-7175-2017)
863 2017, 2017.

864 Carrico, C. M., P. Kus, M. J. Rood, P. K. Quinn, and T. S. Bates, Mixtures of pollution, dust, sea salt, and volcanic
865 aerosol during ACE-Asia: Radiative properties as a function of relative humidity, *J. Geophys. Res.*, 108, 8650,
866 doi: 10.1029/2003JD003405, D23, 2003.

867 Cattrall, C., Carder, K. L., and Gordon, H. R.: Columnar aerosol single-scattering albedo and phase function re-
868 trieved from sky radiance over the ocean: Measurements of Saharan dust, *J. Geophys. Res.–Atmos.*, 108(D9),
869 4287, doi:10.1029/2002JD002497, 2003

870 Chen, G., Ziemba, L. D., Chu, D. A., Thornhill, K. L., Schuster, G. L., Winstead, E. L., Diskin, G. S., Ferrare, R. A.,
871 Burton, S. P., Ismail, S., Kooi, S. A., Omar, A. H., Slusher, D. L., Kleb, M. M., Reid, J. S., Twohy, C. H., Zhang,
872 H., and Anderson, B. E.: Observations of Saharan dust microphysical and optical properties from the Eastern
873 Atlantic during NAMMA airborne field campaign, *Atmos. Chem. Phys.*, 11, 723–740,
874 <https://doi.org/10.5194/acp-11-723-2011>, 2011.

875 Chou, C., Formenti, P., Maille, M., Ausset, P., Helas, G., Harrison, M., and Osborne, S.: Size distribution, shape,
876 and composition of mineral dust aerosols collected during the African Monsoon Multidisciplinary Analysis Spe-
877 cial Observation Period 0: Dust and Biomass-Burning Experiment field campaign in Niger, January 2006, *J.*
878 *Geophys. Res.*, 113, D00C10, doi:10.1029/2008jd009897, 2008.

879 Claquin, T., Schulz, M., and Balkanski, Y.: Modeling the mineralogy of atmospheric dust sources, *J. Geophys.*
880 *Res.*, 104, 22 243– 22 256, 1999.

881 Clarke, A. D., Shinozuka, Y. V., Kapustin, N., Howell, S., Huebert, B., Doherty, S., Anderson, T., Covert, D., Ander-
882 son, J., Hua, X., Moore II, K. G., McNaughton, C., Carmichael, G., and Weber, R.: Size distributions and mix-
883 tures of dust and black carbon aerosol in Asian outflow: Physiochemistry and optical properties, *J. Geophys.*
884 *Res.*, 109, D15S09, doi:10.1029/2003JD004378, 2004.

885 Colarco, P. R., Nowotnick, E. P., Randles, C. A., Yi, B., Yang, P., Kim, K.-M., Smith, J. A., and Bardeen, C. G.:
886 Impact of radiatively interactive dust aerosols in the NASA GEOS-5 climate model: Sensitivity to dust particle
887 shape and refractive index, *J. Geophys. Res. Atmos.*, 119, 753–786, doi: 10.1002/2013JD020046, 2014.

888 Collaud Coen, M., Weingartner, E., Apituley, A., Ceburnis, D., Fierz-Schmidhauser, R., Flentje, H., Henzing, J. S.,
889 Jennings, S. G., Moerman, M., Petzold, A., Schmid, O., and Baltensperger, U.: Minimizing light absorption
890 measurement artifacts of the Aethalometer: evaluation of five correction algorithms, *Atmos. Meas. Tech.*, 3,
891 457–474, doi:10.5194/amt-3-457-2010, 2010.

892 d'Almeida, G. A., Koepke, P., and Shettle, E.P.: *Atmospheric Aerosols: Global Climatology and Radiative Charac-*
893 *teristics*, A. Deepak Publishing, 561 pp., 1991.

894 Das, S., S. Dey, S. K. Dash, G. Giuliani, and F. Solmon: Dust aerosol feedback on the Indian summer monsoon:
895 Sensitivity to absorption property, *J. Geophys. Res. Atmos.*, 120, 9642–9652, doi: 10.1002/2015JD023589,
896 2015.

897 Denjean, C., Formenti, P., Picquet-Varrault, B., Katrib, Y., Pangui, E., Zapf, P., and Doussin, J. F.: A new experi-
898 mental approach to study the hygroscopic and optical properties of aerosols: application to ammonium sulphate
899 particles, *Atmos. Meas. Tech.*, 7, 183–197, doi:10.5194/amt-7-183-2014, 2014.

900 Denjean, C., Cassola, F., Mazzino, A., Triquet, S., Chevaillier, S., Grand, N., Bourriane, T., Momboisse, G., Sel-
901 legri, K., Schwarzenbock, A., Freney, E., Mallet, M., and Formenti, P.: Size distribution and optical properties
902 of mineral dust aerosols transported in the western Mediterranean, *Atmos. Chem. Phys.*, 16, 1081–1104,
903 <https://doi.org/10.5194/acp-16-1081-2016>, 2016a.

904 Denjean, C., Formenti, P., Desboeufs, K., Chevaillier, S., Triquet, S., Maillé, M., Cazaunau, M., Laurent, B., Mayol-
905 Bracero, O. L., Vallejo, P., Quiñones, M., Gutierrez-Molina, I. E., Cassola, F., Prati, P., Andrews, E., and Ogren,
906 J.: Size distribution and optical properties of African mineral dust after intercontinental transport, *J. Geophys.*
907 *Res.–Atmos.*, 121, 7117–7138, <https://doi.org/10.1002/2016JD024783>, 2016b.

908 Derimian, Y., Karnieli, A., Kaufman, Y. J., Andreae, M. O., Andreae, T. W., Dubovik, O., Maenhaut, W., and Koren,
909 I.: The role of iron and black carbon in aerosol light absorption, *Atmos. Chem. Phys.*, 8, 3623–3637, 2008.

910 Di Biagio, C., Formenti, P., Styler, S. A., Pangui, E., and Doussin, J.-F.: Laboratory chamber measurements of the
911 longwave extinction spectra and complex refractive indices of African and Asian mineral dusts, *Geophys. Res.*
912 *Letts.*, 41, 6289–6297, doi:10.1002/2014GL060213, 2014a.

913 Di Biagio, C., Boucher, H., Caqueneau, S., Chevaillier, S., Cuesta, J., and Formenti, P.: Variability of the infrared
914 complex refractive index of African mineral dust: experimental estimation and implications for radiative transfer
915 and satellite remote sensing, *Atmos. Chem. Phys.*, 14, 11093–11116, [https://doi.org/10.5194/acp-14-11093-](https://doi.org/10.5194/acp-14-11093-2014)
916 [2014](https://doi.org/10.5194/acp-14-11093-2014), 2014b.

917 Di Biagio, C., Formenti, P., Balkanski, Y., Caponi, L., Cazaunau, M., Pangui, E., Journet, E., Nowak, S., Caqueneau,
918 S., Andreae, M. O., Kandler, K., Saeed, T., Piketh, S., Seibert, D., Williams, E., and Doussin, J.-F.: Global
919 scale variability of the mineral dust long-wave refractive index: a new dataset of in situ measurements for
920 climate modeling and remote sensing, *Atmos. Chem. Phys.*, 17, 1901–1929, [https://doi.org/10.5194/acp-17-](https://doi.org/10.5194/acp-17-1901-2017)
921 [1901-2017](https://doi.org/10.5194/acp-17-1901-2017), 2017a.

922 Di Biagio, C., Formenti, P., Cazaunau, M., Pangui, E., Marchand, N., and Doussin, J.-F.: Aethalometer multiple
923 scattering correction C_{ref} for mineral dust aerosols, *Atmos. Meas. Tech.*, 10, 2923–2939,
924 <https://doi.org/10.5194/amt-10-2923-2017>, 2017b.

925 Dubovik, O., Holben, B. N., and Eck, T. F. et al.: Variability of absorption and optical properties of key aerosol types
926 observed in worldwide locations, *J. Atmos. Sci.*, 59, 590–608, 2002. Dunion, J. P., and C. S. Velden: The impact
927 of the Saharan air layer on Atlantic tropical cyclone activity, *Bull. Am. Meteorol. Soc.*, 85(3), 353. Mete-
928 oro:10.1175/BAMS-85-3-353, 2004.

929 Engelbrecht, J. P., Moosmüller, H., Pincock, S., Jayanty, R. K. M., Lersch, T., and Casuccio, G.: Technical note:
930 Mineralogical, chemical, morphological, and optical interrelationships of mineral dust re-suspensions, *Atmos.*
931 *Chem. Phys.*, 16, 10809–10830, <https://doi.org/10.5194/acp-16-10809-2016>, 2016. Feng, Q., P. Yang, G. W.
932 Kattawar, C. N. Hsu, S.-C. Tsay, and I. Laszlo: Effects of particle nonsphericity and radiation polarization on
933 retrieving dust properties from MODIS observations, *J. Aerosol Sci.*, 40(9), 776–789, doi:10.1016/j.jaero-
934 sci.2009.05.001, 2009.

935 Flores, J. M., Trainic, M., Borrmann, S., and Rudich, Y.: Effective broadband refractive index retrieval by a white
936 light optical particle counter, *Phys. Chem. Chem. Phys.*, 11, 7943–7950, 2009.

937 Formenti, P., Andreae, M. O., Lange, L., Roberts, G., Cafmeyer, J., Rajta, I., Maenhaut, W., Holben, B. N., Artaxo,
938 P., and Lelieveld, J.: Saharan dust in Brazil and Suriname during the Large-Scale Biosphere-Atmosphere
939 Experiment in Amazonia (LBA) – Cooperative LBA Regional Experiment (CLAIRE) in March 1998, *J. Geophys.*
940 *Res.*, 106, 14919–14934, <https://doi.org/10.1029/2000jd900827>, 2001.

941 Formenti, P., Rajot, J. L., Desboeufs, K., Said, F., Grand, N., Chevaillier, S., and Schmechtig, C.: Airborne obser-
942 vations of mineral dust over western Africa in the summer Monsoon season: spatial and vertical variability of
943 physico-chemical and optical properties, *Atmos. Chem. Phys.*, 11, 6387–6410, doi:10.5194/acp-11-6387-
944 2011, 2011.

945 Formenti, P., Caqueneau, S., Desboeufs, K., Klaver, A., Chevaillier, S., Journet, E., and Rajot, J. L.: Mapping the
946 physicochemical properties of mineral dust in western Africa: mineralogical composition, *Atmos. Chem. Phys.*,
947 14, 10663–10686, <https://doi.org/10.5194/acp-14-10663-2014>, 2014a.

948 Formenti, P., Caqueneau, S., Chevaillier, S., Klaver, A., Desboeufs, K., Rajot, J. L., Belin, S., and Briois, V.: Domi-
949 nance of goethite over hematite in iron oxides of mineral dust from western Africa: quantitative partitioning by
950 X-ray Absorption Spectroscopy, *J. Geophys. Res.–Atmos.*, 119, 12740–12754,
951 <https://doi.org/10.1002/2014JD021668>, 2014b.

952 Gasteiger, J., Wiegner, M., Groß, S., Freudenthaler, V., Toledano, C., Tesche, M., and Kandler, K.: Modelling lidar-
953 relevant optical properties of complex mineral dust aerosols, *Tellus B*, 63, 725–741,
954 <https://doi.org/10.1111/j.1600-0889.2011.00559.x>, 2011.

955 Ginoux, P., Prospero, J. M., Gill, T. E., Hsu, N. C., and Zhao, M.: Global-scale attribution of anthropogenic and
956 natural dust sources and their emission rates based on MODIS Deep Blue aerosol products, *Rev. Geophys.*,
957 50, RG3005, doi:10.1029/2012RG000388, 2012.

958 Green, R. O.; Mahowald, N. M.; Clark, R. N.; Ehlmann, B. L.; Ginoux, P. A.; Kalashnikova, O. V.; Miller, R. L.; Okin,
959 G.; Painter, T. H.; Pérez García-Pando, C.; Realmuto, V. J.; Swayze, G. A.; Thompson, D. R.; Middleton, E.;
960 Guanter, L.; Ben Dor, E.; Phillips, B. R. (2018) NASA's Earth Surface Mineral Dust Source Investigation. Amer-
961 ican Geophysical Union, Fall Meeting 2018, abstract #A24D-01.

962 Haywood, J., Francis, P., Osborne, S., Glew, M., Loeb, N., Highwood, E., Tanré, D., Myhre, G., Formenti, P., and
963 Hirst, E.: Radiative properties and direct radiative effect of Saharan dust measured by the C-130 aircraft during
964 SHADE: 1. Solar spectrum, *J. Geophys. Res.*, 108(D18), 8577, doi:10.1029/2002JD002687, 2003.

965 Hess, M., Koepke, P., and Schult, I.: Optical properties of aerosols and clouds: The software package OPAC, *Bull.*
966 *Am. Meteorol. Soc.*, 79, 831–844, 1998.

967 Highwood, E. J., and Ryder, C. L.: Radiative effects of dust. In *Mineral Dust: A Key Player in the Earth System*. P.
968 Knippertz, and J.-B.W. Stuut, Eds. Springer, 267–286, doi:10.1007/978-94-017-8978-3_13, 2014.

969 Hsu, N. C., Tsay, S.-C., King, M. D., and Herman, J. R.: Aerosol properties over bright-reflecting source regions,
970 *IEEE T. Geosci. Remote Sens.*, 42, 557–569, 2004.

971 Iwasaka, Y., Shi, G.-Y., Shen, Z., Kim, Y. S., Trochkin, D., Matsuki, A., Zhang, D., Shibata, T., Nagatani, M., and
972 Nakata, H.: Nature of atmospheric aerosols over the desert area in the Asian continent: chemical state and
973 number concentration of particles measured at Dunhuang, China, *Water Air Soil Poll.*, 3, 129–145, 2003

974 Jeong, G. Y., J. Y. Kim, J. Seo, G. M. Kim, H. C. Jin, and Y. Chun: Long-range transport of giant particles in Asian
975 dust identified by physical, mineralogical, and meteorological analysis, *Atmos. Chem. Phys.*, 14(1), 505–521,
976 doi:10.5194/acp-14-505-2014, 2014.

977 Jin, Q., Zang, Z.-L., and Wei, J.: High sensitivity of Indian summer monsoon to Middle East dust absorptive prop-
978 erties, *Sci. Rep.*, 6:30690, doi: 10.1038/srep30690, 2016.

979 Johnson, B. T. and Osborne, S. R.: Physical and optical properties of mineral dust aerosol measured by aircraft
980 during the GERBILS campaign. *Q.J.R. Meteorol. Soc.*, 137: 1117–1130. doi:10.1002/qj.777, 2011.

981 Journet, E., Balkanski, Y., and Harrison, S. P.: A new data set of soil mineralogy for dust-cycle modeling, *Atmos.*
982 *Chem. Phys.*, 14, 3801–3816, doi:10.5194/acp-14-3801-2014, 2014.

983 Kalashnikova, O. V. and Sokolik, I. N.: Modeling the radiative properties of nonspherical soil-derived mineral aer-
984 osols, *J. Quant. Spectrosc. Ra.*, 87, 137–166, 2004.

985 Kandler, K., Schütz, L., Deutscher, C., Ebert, M., Hofmann, H., Jäckel, S., Jaenicke, R., Knippertz, P., Lieke, K.,
986 Massling, A., Petzold, A., Schladitz, A., Weinzierl, B., Wiedensohler, A., Zorn, S., and Weinbruch, S.: Size dis-
987 tribution, mass concentration, chemical and mineralogical composition and derived optical parameters of the
988 boundary layer aerosol at Tinfou, Morocco, during SAMUM 2006, *Tellus B*, 61, 32–50, doi:10.1111/j.1600-
989 0889.2008.00385.x, 2009.

990 Karickhoff, S.W. and Bailey, G.W. 1973. Optical absorption spectra of clay minerals. *Clay Clay Miner.*, 21, 59–
991 70. Kaufman, Y. J.: Satellite sensing of aerosol absorption, *J. Geophys. Res.*, 92, 4307–4317, 1987.

992 Kaufman, Y. J., Tanré, D., Dubovik, O., Karnieli, A., and Remer, L. A.: Absorption of sunlight by dust as inferred
993 from satellite and ground-based remote sensing, *Geophys. Res. Lett.*, 28, 1479–1482, 2001.

994 Koepke, P., Gasteiger, J., and Hess, M.: Technical Note: Optical properties of desert aerosol with non-spherical
995 mineral particles: data incorporated to OPAC, *Atmos. Chem. Phys.*, 15, 5947–5956,
996 <https://doi.org/10.5194/acp-15-5947-2015>, 2015.

997 Kok, J.F., D.A. Ridley, Q. Zhou, R.L. Miller, C. Zhao, C.L. Heald, D.S. Ward, S. Albani, and K. Haustein: Smaller
998 desert dust cooling effect estimated from analysis of dust size and abundance. *Nature Geosci.*, 10, no. 4, 274–
999 278, doi:10.1038/ngeo2912, 2017.

1000 Konaré, A., Zakey, A. S., Solmon, F., Giorgi, F., Rauscher, S., Ibrah, S., and Bi, X.: A regional climate modeling
1001 study of the effect of desert dust on the West African monsoon, *J. Geophys. Res.*, 113, D12206,
1002 doi:10.1029/2007JD009322, 2008.

1003 Koven, C.D., and Fung, I.: Inferring dust composition from wavelength-dependent absorption in Aerosol Robotic
1004 Network (AERONET) data. *J Geophys Res* 111, D14205. doi:10.1029/2005JD006678, 2006.

1005 Lafon, S., Sokolik, I. N., Rajot, J. L., Caquineau, S., and Gaudichet, A.: Characterization of iron oxides in mineral
1006 dust aerosols: Implications for light absorption, *J. Geophys. Res.*, 111, D21207, doi:10.1029/2005jd007016, 2006.

1007 Liao, H. and Seinfeld, J. H.: Radiative forcing by mineral dust aerosols: sensitivity to key variables, *J. Geophys.*
1008 *Res.*, 103(D24), 31 637–31 646, doi:10.1029/1998JD200036, 1998.

1009 Lide, D. R.: *CRC Handbook of Chemistry and Physics 1991–1992*, CRC Press, Boca Raton, Florida, 1992.

1010 Linke, C., Möhler, O., Veres, A., Mohácsi, A., Bozóki, Z., Szabó, G., and Schnaiter, M., Optical properties and
1011 mineralogical composition of different Saharan mineral dust samples: a laboratory study, *Atmos. Chem. Phys.*,
1012 6, 3315–3323, 2006.

1013 Lu, H., Wei, W., Liu, M., Wu, X., Mou, S., and Han, Q.: Quantification and semi-quantification of iron-oxide minerals
1014 in aerosol particles in the hinterland of Taklimakan Desert, *Scientia Geographica Sinica*, 31, 969–975, 2011.

1015 Maring, H., Savoie, D. L., Izaguirre, M. A., McCormick, C., Arimoto, R., Prospero, J. M., and Pilinis, C.: Aerosol
1016 physical and optical properties and their relationship to aerosol composition in the free troposphere at izana,
1017 tenerife, canary islands, during July 1995, *J. Geophys. Res.–Atmos.*, 105, 14677–14700, 2000.

1018 Maring, H., Savoie, D. L., Izaguirre, M. A., Custals, L., and Reid, J. S.: Mineral dust aerosol size distribution change
1019 during atmospheric transport, *J. Geophys. Res.*, 108, 8592, doi:10.1029/2002jd002536, 2003.

1020 McConnell, C. L., Highwood, E. J., Coe, H., Formenti, P., Anderson, B., Osborne, S., Nava, S., Desboeufs, K.,
1021 Chen, G., and Harrison, M. A. J.: Seasonal variations of the physical and optical characteristics of Saharan
1022 dust: Results from the Dust Outflow and Deposition to the Ocean (DODO) experiment, *J. Geophys. Res.*, 113,
1023 D14S05, doi:10.1029/2007jd009606, 2008.

1024 McConnell, C. L., Formenti, P., Highwood, E. J., and Harrison, M. A. J.: Using aircraft measurements to determine
1025 the refractive index of Saharan dust during the DODO Experiments, *Atmos. Chem. Phys.*, 10, 3081–3098,
1026 doi:10.5194/acp-10-3081-2010, 2010.

1027 Miller, R. L., I. Tegen, and J. Perlwitz: Surface radiative forcing by soil dust aerosols and the hydrologic cycle, *J.*
1028 *Geophys. Res.*, 109, D04203, doi:10.1029/2003JD004085, 2004.

1029 Miller, R. L., Knippertz, P., Pérez García-Pando, C., Perlwitz, J. P., and Tegen, I.: Impact of dust radiative forcing
1030 upon climate. In *Mineral Dust: A Key Player in the Earth System*. P. Knippertz, and J.–B.W. Stuut, Eds. Springer,
1031 327–357, doi:10.1007/978-94-017-8978-3_13, 2014.

1032 Mishchenko, M., A. Lacis, B. Carlson, and L. Travis: Nonsphericity of dust-like tropospheric aerosols—Implications
1033 for aerosol remotesensing and climate modeling, *Geophys. Res. Lett.*, 22(9), 1077–1080, 1995. Mogili, P. K.,
1034 Yang, K. H., Young, M. A., Kleiber, P. D., and Grassian, V. H.: Environmental aerosol chamber studies of
1035 extinction spectra of mineral dust aerosol components: Broadband IR–UV extinction spectra, *J. Geophys. Res.–*
1036 *Atmos.*, 112, D21204, doi:10.1029/2007JD008890, 2007.

1037 Moosmüller, H., Engelbrecht, J. P., Skiba, M., Frey, G., Chakrabarty, R.K., and Arnott, W.P., Single scattering
1038 albedo of fine mineral dust aerosols controlled by iron concentration, *J. Geophys. Res.*, 117, D11210,
1039 doi:10.1029/2011JD016909, 2012.

1040 Müller, T., Schladitz, A., Massling, A., Kaaden, N., Kandler, K., and coauthors: Spectral absorption coefficients and
1041 imaginary parts of refractive indices of Saharan dust during SAMUM–1. *Tellus 61B*, 79–95, 2009.

1042 Müller, T., Schladitz, A., Kandler, K., and Wiedensohler, A.: Spectral particle absorption coefficients, single scat-
1043 tering albedos and imaginary parts of refractive indices from ground based in situ measurements at Cape Verde
1044 Island during SAMUM–2, *Tellus B*, 63, 573–588, doi:10.1111/j.1600-0889.2011.00572.x, 2011.

1045 Myhre, G. and Stordal, F.: Global sensitivity experiments of the radiative forcing due to mineral aerosols, *J. Ge-*
1046 *ophys. Res.*, 106(D16), 18 193–18 204, doi:10.1029/2000JD900536, 2001.

1047 Nickovic, S., Vukovic, A., Vujadinovic, M., Djurdjevic, V., and Pejanovic, G.: Technical Note: High-resolution min-
1048 eralogical database of dust-productive soils for atmospheric dust modeling, *Atmos. Chem. Phys.*, 12, 845–855,
1049 doi:10.5194/acp-12-845-2012, 2012.

1050 Nousiainen, T. and Kandler, K.: Light scattering by atmospheric mineral dust particles, in: *Light Scattering Reviews*
1051 9, edited by: Kokhanovsky, A. A., Springer Praxis Books, Springer, Berlin, Heidelberg, 3–52, doi:10.1007/978-
1052 3-642-37985-7, 2015.

1053 Okada, K., Heintzenberg, J., Kai, K., Qin, Y., 2001. Shape of atmospheric mineral particles collected in three Chi-
1054 nese arid-regions. *Geophys. Res. Lett.* 28 (16), 3123–3126

1055 Osborne, S.R., Johnson, B.T., Haywood, J.M., Baran, A.J., Harrison, M.A.J., and McConnell, C.L.: Physical and
1056 optical properties of mineral dust aerosol during the Dust and Biomass-burning Experiment, *J. Geophys. Res.*,
1057 113, D00C03, doi:10.1029/2007jd009551, 2008.

1058 Otto, S., Bierwirth, E., Weinzierl, B., Kandler, K., Esselborn, M., Tesche, M., Schladitz, A., Wendisch, M., and Tra-
1059 utmann, T.: Solar radiative effects of a Saharan dust plume observed during SAMUM assuming spheroidal
1060 model particles, *Tellus B*, 61, 270–296, doi:10.1111/j.1600-0889.2008.00389.x, 2009.

1061 Patterson, E.M., Filette, D. A., and Stockton, B. H.: Complex index of refraction between 300 and 700 nm for
1062 Saharan aerosols, *J. Geophys. Res.*, 82, 3153–3160, 1977.

1063 Perlwitz, J. P., Pérez García-Pando, C., and Miller, R. L.: Predicting the mineral composition of dust aerosols –
1064 Part 1: Representing key processes, *Atmos. Chem. Phys.*, 15, 11593–11627, [https://doi.org/10.5194/acp-15-](https://doi.org/10.5194/acp-15-11593-2015)
1065 11593-2015, 2015a.

1066 Perlwitz, J. P., Pérez García-Pando, C., and Miller, R. L.: Predicting the mineral composition of dust aerosols –
1067 Part 2: Model evaluation and identification of key processes with observations, *Atmos. Chem. Phys.*, 15, 11629–
1068 11652, <https://doi.org/10.5194/acp-15-11629-2015>, 2015b.

1069 Petzold, A., Schloesser, H., Sheridan, P. J., Arnott, W. P., Ogren, J. A., and Virkkula, A.: Evaluation of Multi-angle
1070 Absorption Photometry for Measuring Aerosol Light Absorption, *Aerosol Sci. Technol.*, 39, 40–51, 2005.

1071 Petzold, A., Rasp, K., Weinzierl, B., Esselborn, M., Hamburger, T., Dornbrack, A., Kandler, K., Schutz, L., Knip-
1072 pertz, P., Fiebig, M., Virkkula, A., Saharan dust absorption and refractive index from aircraft-based observa-
1073 tions during SAMUM 2006, *Tellus B* 61: 118–130, 2009.

1074 Petzold, A., Onasch, T., Kebejian, P., and Freedman, A.: Intercomparison of a Cavity Attenuated Phase Shift-
1075 based extinction monitor (CAPS PMex) with an integrating nephelometer and a filter-based absorption monitor,
1076 *Atmos. Meas. Tech.*, 6, 1141–1151, doi:10.5194/amt-6-1141-2013, 2013. Räsänen, P., P. Haapanala, C. E.
1077 Chung, M. Kahnert, R. Makkonen, J. Tonttila, and T. Nousiainen: Impact of dust particle non-sphericity on
1078 climate simulations, *Q. J. R. Meteorol. Soc.*, 139, 2222–2232, doi:10.1002/qj.2084, 2012.

1079 Räsänen, P., P. Haapanala, C. E. Chung, M. Kahnert, R. Makkonen, J. Tonttila, and T. Nousiainen: Impact of dust
1080 particle non-sphericity on climate simulations, *Q. J. R. Meteorol. Soc.*, 139, 2222–2232, doi:10.1002/qj.2084,
1081 2012.

1082 Rajot, J. L., Formenti, P., Alfaro, S., Desboeufs, K., Chevaillier, S., Chatenet, B., Gaudichet, A., Journet, E., Marti-
1083 corena, B., Triquet, S., Maman, A., Mouget, N., and Zakou, A.: AMMA dust experiment: an overview of meas-
1084 urements performed during the dry season special observation period (SOP0) at the Banizoumbou (Niger)
1085 supersite, *J. Geophys. Res.*, 113, D00C14, doi:10.1029/2008jd009906, 2008.

1086 Redmond, H. E., Dial, K. D., and Thompson, J.E.: Light scattering and absorption by wind-blown dust: theory,
1087 measurement and recent data, *Aeolian Res.*, 2, 5–26, 2010.

1088 Reid, E. A., Reid, J. S., Meier, M. M., Dunlap, M. R., Cliff, S. S., Broumas, A., Perry, K., and Maring, H.: Charac-
1089 terization of African dust transported to Puerto Rico by individual particle and size segregated bulk analysis, *J.*
1090 *Geophys. Res.*, 108, 8591, doi:10.1029/2002jd002935, 2003.

1091 Ridley, D. A., Heald, C. L., Kok, J. F., and Zhao, C.: An observationally constrained estimate of global dust aerosol
1092 optical depth, *Atmos. Chem. Phys.*, 16, 15097–15117, <https://doi.org/10.5194/acp-16-15097-2016>, 2016.

1093 Rocha-Lima, A., Martins, J. V., Remer, L. A., Todd, M., Marsham, J. H., Engelstaedter, S., Ryder, C. L., Cavazos-
1094 Guerra, C., Artaxo, P., Colarco, P., and Washington, R.: A detailed characterization of the Saharan dust col-
1095 lected during the Fennec campaign in 2011: in situ ground-based and laboratory measurements, *Atmos. Chem.*
1096 *Phys.*, 18, 1023–1043, <https://doi.org/10.5194/acp-18-1023-2018>, 2018.

1097 Ryder, C. L., Highwood, E. J., Rosenberg, P. D., Trembath, J., Brooke, J. K., Bart, M., Dean, A., Crosier, J., Dorsey,
1098 J., Brindley, H., Banks, J., Marsham, J. H., McQuaid, J. B., Sodemann, H., and Washington, R.: Optical prop-
1099 erties of Saharan dust aerosol and contribution from the coarse mode as measured during the Fennec 2011
1100 aircraft campaign, *Atmos. Chem. Phys.*, 13, 303–325, doi:10.5194/acp-13-303-2013, 2013a.

1101 Ryder, C. L., Highwood, E. J., Lai, T. M., Sodemann, H., and Marsham J. H.: Impact of atmospheric transport on
1102 the evolution of microphysical and optical properties of Saharan dust, *Geophys. Res. Lett.*, 40, 2433–2438, doi:
1103 10.1002/grl.50482, 2013b.

1104 Ryder, C. L., Marengo, F., Brooke, J. K., Estelles, V., Cotton, R., Formenti, P., McQuaid, J. B., Price, H. C., Liu, D.,
1105 Ausset, P., Rosenberg, P. D., Taylor, J. W., Choularton, T., Bower, K., Coe, H., Gallagher, M., Crosier, J., Lloyd,
1106 G., Highwood, E. J., and Murray, B. J.: Coarse-mode mineral dust size distributions, composition and optical
1107 properties from AER-D aircraft measurements over the tropical eastern Atlantic, *Atmos. Chem. Phys.*, 18,
1108 17225–17257, <https://doi.org/10.5194/acp-18-17225-2018>, 2018.

1109 Samset, B. H., Stjern, C. W., Andrews, E., Kahn, R. A., Myhre, G., Schulz, M., and Schuster, G. L.: Aerosol Ab-
1110 sorption: Progress Towards Global and Regional Constraints, *Curr. Clim. Change Rep.*, 4, 65–83, 2018.

1111 Saturno, J., Pöhlker, C., Massabo, D., Brito, J., Carbone, S., Cheng, Y. F., Chi, X. G., Ditas, F., de Angelis, I. H.,
1112 Moran-Zuloaga, D., Pöhlker, M. L., Rizzo, L. V., Walter, D., Wang, Q. Q., Artaxo, P., Prati, P., and Andreae,
1113 M. O., Comparison of different Aethalometer correction schemes and a reference multi-wavelength absorption
1114 technique for ambient aerosol data: *Atmos. Meas. Tech.*, 10, 2837–2850, doi:10.5194/amt-10-2837-2017,
1115 2017.

1116 Scanza, R. A., Mahowald, N., Ghan, S., Zender, C. S., Kok, J. F., Liu, X., Zhang, Y., and Albani, S.: Modeling dust
1117 as component minerals in the Community Atmosphere Model: development of framework and impact on radi-
1118 ative forcing, *Atmos. Chem. Phys.*, 15, 537–561, doi:10.5194/acp-15-537-2015, 2015.

1119 Scheuvens, D., Schütz, L., Kandler, K., Ebert, M., and Weinbruch, S.: Bulk composition of northern African dust
1120 and its source sediments – A compilation, *Earth-Sci. Rev.*, 116, 170–194, [https://doi.org/10.1016/j.earsci-](https://doi.org/10.1016/j.earsci-rev.2012.08.005)
1121 [rev.2012.08.005](https://doi.org/10.1016/j.earsci-rev.2012.08.005), 2013.

1122 Schladitz, A., Müller, T., Kaaden, N., Massling, A., Kandler, K., Ebert, M., Weinbruch, S., Deutscher, C., and
1123 Wiedensohler, A.: In situ measurements of optical properties at Tinfou (Morocco) during the Saharan Mineral
1124 Dust Experiment SAMUM 2006, *Tellus B*, 61, 64–78, doi:10.1111/j.1600-0889.2008.00397.x, 2009.

1125 Shen, Z., Cao, J., Zhang, X., Arimoto, R., Ji, J., Balsam, W., Wang, Y., Zhang, R., and Li, X.: Spectroscopic analysis
1126 of iron-oxide minerals in aerosol particles from northern China, *Sci. Total Environ.*, 367, 899–907, 2006.

1127 Shettle, E. P., and Fenn, R.W.: Models for the Aerosols of the Lower Atmosphere and the Effects of Humidity
1128 Variations on Their Optical Properties, AFGL-TR-79-0214, ADA085951, 1979.

1129 Shin, S.–K., Tesche, M., Kim, K., Kezoudi, M., Tatarov, B., Müller, D., and Noh, Y.: On the spectral depolarisation
1130 and lidar ratio of mineral dust provided in the AERONET version 3 inversion product, *Atmos. Chem. Phys.*, 18,
1131 12735–12746, <https://doi.org/10.5194/acp-18-12735-2018>, 2018.

1132 Sinyuk, A., Torres, O., and Dubovik, O., Combined use of satellite and surface observations to infer the imaginary
1133 part of refractive index of Saharan dust, *Geophys. Res. Lett.*, 30(2), 1081, doi:10.1029/2002GL016189, 2003.

1134 Sokolik, I., and Toon, O.: Incorporation of mineralogical composition into models of the radiative properties of min-
1135 eral aerosol from UV to IR wavelengths, *J. Geophys. Res.*, 104(D8), 9423–9444, 1999.

1136 Sokolik, I.N., Andronova, A.V., and Jonhson, T.C.: Complex refractive index of atmospheric dust aerosols, *Atmos.*
1137 *Environ.*, 16, 2495–2502, 1993.

1138 Solmon, F., Mallet, M., Elguindi, N., Giorgi, F., Zakey, A. and Konaré, A.: Dust aerosol impact on regional precipi-
1139 tation over western Africa, mechanisms and sensitivity to absorption properties, *Geophys. Res. Lett.*, 35,
1140 L24705, doi:10.1029/2008GL035900, 2008. Sorribas, M., Olmo, F. J., Quirantes, A., Lyamani, H., Gil-Ojeda,
1141 M., Alados-Arboledas, L. and Horvath, H. (2015), Role of spheroidal particles in closure studies for aerosol
1142 microphysical–optical properties. *Q.J.R. Meteorol. Soc.*, 141: 2700–2707. doi:[10.1002/qj.2557](https://doi.org/10.1002/qj.2557).

1143 Stegmann, P. G., Yang, P., A regional, size–dependent, and causal effective medium model for Asian and Saharan
1144 mineral dust refractive index spectra, *J. Aer. Sci.*, 114, 327–341, 2017.

1145 Strong, J. D. O., Vecchi, G. A., & Ginoux, P.: The climatological effect of Saharan dust on global tropical cyclones
1146 in a fully coupled GCM. *Journal of Geophysical Research: Atmospheres*, 123, 5538–5559. [https://doi-](https://doi-org.insu.bib.cnrs.fr/10.1029/2017JD027808)
1147 [org.insu.bib.cnrs.fr/10.1029/2017JD027808](https://doi-org.insu.bib.cnrs.fr/10.1029/2017JD027808), 2018

1148 Su, L., and Toon O.B.: Saharan and Asian dust: similarities and differences determined by CALIPSO, AERONET,
1149 and a coupled climate–aerosol microphysical model, *Atmos. Chem. Phys.*; 11, 3263–3280, 2011.

1150 Todd, M. C., R. Washington, J. V. Martins, O. Dubovik, G. Lizcano, S. M'Bainayel, and S. Engelstaedter, Mineral
1151 dust emission from the Bodélé´ Depression, northern Chad, during BoDEx 2005, *J. Geophys. Res.*, 112,
1152 D06207, doi:10.1029/2006JD007170, 2007.

1153 Toon, O. B., Pollack, J. B., and Khare, B. N.: The optical constants of several atmospheric aerosol species: am-
1154 monium sulphate, aluminum oxide, and sodium chloride, *J. Geophys. Res.*, 81, 5733–5748, 1976.

1155 Uno, I., K. Eguchi, K. Yumimoto, T. Takemura, A. Shimizu, M. Uematsu, Z. Liu, Z. Wang, Y. Hara, and N. Sugimoto,
1156 Asian dust transported one full circuit around the globe, *Nat. Geosci.*, 2, 557–560, doi:10.1038/ngeo583, 2009.

1157 Vinoj, V. et al. Short–term modulation of Indian summer monsoon rainfall by West Asian dust. *Nature Geoscience*
1158 7, 308–313, 2014.

1159 Volz, F. E.: Longwave refractive index of atmospheric aerosol substances, *Appl. Optics*, 11, 755–759, 1972.

1160 Wang, J., Doussin, J. F., Perrier, S., Perraudin, E., Katrib, Y., Pangui, E., and Picquet–Varrault, B.: Design of a
1161 new multi–phase experimental simulation chamber for atmospheric photo-smog, aerosol and cloud chemistry
1162 research, *Atmos. Meas. Tech.*, 4, 2465–2494, 2011.

1163 Wagner, R., Ajtai, T., Kandler, K., Lieke, K., Linke, C., Müller, T., Schnaiter, M., and Vragel, M.: Complex refractive
1164 indices of Saharan dust samples at visible and near UV wavelengths: a laboratory study, *Atmos. Chem. Phys.*,
1165 12, 2491–2512, doi:10.5194/acp-12-2491-2012, 2012.

1166 Weingartner, E., Saathoff, H., Schnaiter, M., Streit, N., Bitnar, B., and Baltensperger, U.: Absorption of light by soot
1167 particles: determination of the absorption coefficient by means of aethalometers, *J. Aerosol Sci.*, 34, 1445–
1168 1463, 2003.

1169 Weinzierl, B., Petzold, A., Esselborn, M., Wirth, M., Rasp, K., Kandler, K., Schutz, L., Koepke, P., and Fiebig, M.:
1170 Airborne measurements of dust layer properties, particle size distribution and mixing state of Saharan dust
1171 during SAMUM 2006, *Tellus*, 61B, 96–117, doi:10.1111/j.1600-0889.2008.00392.x, 2009.

1172 Weinzierl, B., Sauer, D., Esselborn, M., Petzold, A., Veira, A., Rose, M., Mund, S., Wirth, M., Ansmann, A., Tesche,
1173 M., Gross, S., and Freudenthaler, V.: Microphysical and optical properties of dust and tropical biomass burning
1174 aerosol layers in the Cape Verde region—an overview of the airborne in situ and lidar measurements during
1175 SAMUM–2, *Tellus B*, 63, 589–618, doi:10.1111/j.1600-0889.2011.00566.x, 2011.

1176 Weinzierl, B. et al. (2009), Airborne measurements of dust layer properties, particle size distribution and mixing
1177 state of Saharan dust during SAMUM 2006. *Tellus*– 61B, 96–117.

1178 Yi, B., C. N. Hsu, P. Yang, and S.–C. Tsay: Radiative transfer simulation of dust–like aerosols uncertainties from
1179 particle shape and refractive index, *J. Aerosol Sci.*, 42(10), 631–644, doi:10.1016/j.jaerosci.2011.06.008, 2011.

1180 Yoshida, M. and Murakami, H.: Dust absorption averaged over the Sahara inferred from moderate resolution im-
1181 aging spectroradiometer data, *Appl. Opt.*, 47, 1995–2003, 2008.

1182 Yoshioka, M., Mahowald, N.M., Conley, A.J., Collins, W.D., Fillmore, D.W., Zender, C.S., and Coleman, D.B.: Im-
1183 pact of desert dust radiative forcing on sahel precipitation: Relative importance of dust compared to sea surface
1184 temperature variations, vegetation changes, and greenhouse gas warming, *J. Clim.*, 20, 1445– 1467, 2007.

1185
1186
1187
1188

1189 **Table 1.** Measured and retrieved quantities and their estimated relative uncertainties. For further de-
 1190 tails, refer to Sect. 2, as well DB17 and C17.

1191

Parameter	Time resolution	Relative uncertainty	Uncertainty calculation	Comments
Scattering coefficient at 450, 550, and 700 nm, $\beta_{sca}(\lambda)$	10-min data	5–12%	Quadratic combination of photon counting and gas calibration uncertainty (5%), angular corrections uncertainty (<5%) and standard deviation over 10-min intervals (2–10%).	The uncertainty on $\beta_{sca}(\lambda)$ usually decreases with increasing dust residence time in the chamber as a result of the reduction of the coarse component.
Absorption coefficient at 370, 470, 520, 590, 660, 880, and 950 nm, $\beta_{abs}(\lambda)$	10-min data	22–30% at 370 nm 23–87% at 950 nm	Error propagation formula ¹ on Eq. (2) considering the uncertainties on $\beta_{ATT}(\lambda)$ from 10-min fitting procedure (error propagation formula ¹ on Eq. 1, ~20%), and uncertainties on $\alpha(\lambda)$ (1%), $\beta_{sca}(\lambda)$ (5–12%), C_{ref} (10%), and R (1–10%).	
Extinction coefficient, $\beta_{ext}(\lambda) = \beta_{sca}(\lambda) + \beta_{abs}(\lambda)$	10-min data	~25%	Sum of $\beta_{sca}(\lambda)$ and $\beta_{abs}(\lambda)$ uncertainties	
Single Scattering Albedo, SSA (λ) = $\beta_{sca}(\lambda) / (\beta_{sca}(\lambda) + \beta_{abs}(\lambda))$	10-min data	9–12%	Error propagation formula ¹ considering single uncertainties on $\beta_{sca}(\lambda)$ and $\beta_{abs}(\lambda)$.	
Optical SW Single Scattering Albedo, SSA (λ) = $(1+1/m(\lambda))^{-1}$	Experiment averaged	1–12% at 370 nm 1–3% at 950 nm	Error propagation formula ¹ on Eq. (6) considering the uncertainty on $m(\lambda)$, i.e., the slope of the linear fit between $\beta_{sca}(\lambda)$ and $\beta_{abs}(\lambda)$ over the whole duration of each experiment.	
Complex refractive index ($n-ik$)	10-min data	<5% for n <50% for k	Deviations of the values of n and k retrieved in the sensitivity study (see Sect. 3.2) with respect to those obtained in the first inversions were assumed to correspond to the one standard deviation uncertainty to 10-min retrieved values.	
Complex refractive index ($n-ik$)	Experiment averaged	<8% for n 13–75 % for k	Quadratic combination of the standard deviation of n and k over the experiment and the deviation on the experiment-averaged values between those obtained from central inversions and inversions using input data \pm their uncertainty.	
Size distribution SMPS geometrical diameter (D_g), $D_g = D_m / \chi$	–	~6%	Error propagation formula ¹ considering the uncertainty on the estimated shape factor χ (~6%)	The electrical mobility to geometrical diameter conversion was performed by assuming for dust a dynamic shape factor of 1.75 ± 0.10 , as determined by SMPS–SkyGrimm comparison in their overlapping range (see DB17)

	SkyGrimm geometrical diameter (D_g)	-	<15.2%	Standard deviation of the D_g values obtained for different refractive indices values used in the optical to geometrical conversion	The conversion of optical to geometrical diameters for the SkyGrimm and the WELAS was performed by taking into account the visible complex refractive index of dust aerosols. Optical calculations were computed at the SkyGrimm operating wavelength (0.655 μm) and over the spectral range of the WELAS (0.35 to 0.7 μm) using Mie theory for spherical particles by fixing n at 1.47, 1.50, and 1.53, and by varying k in steps of 0.001 between 0.001 and 0.005. Then D_g is set at the mean ± 1 standard deviation of the values obtained for the different values of n and k (see DB17). Refractive index is assumed to be constant with particle size and wavelength-independent.
	WELAS geometrical diameter (D_g)	-	<7%	The same as for the SkyGrimm	
	$(dN/d\log D)_{\text{SWoptics}}$	10-min data	~20–90%	Error propagation formula ¹ considering the $dN/d\log D_g$ st. dev. over 10-min and the uncertainty on particle loss function along sampling tubes $L(D_g)$ (~50% at 2 μm , ~10% at 8 μm)	The uncertainty of $L(D_g)$ was estimated with a sensitivity study by varying the values of the input parameters to the Particle Loss Calculator software within their uncertainties (see DB17)
	$D_{\text{eff, fine}}$	10-min data	<5%	Deviation obtained by repeating the calculations by using the size distribution \pm its uncertainty.	
	$D_{\text{eff, coarse}}$	10-min data	5–40%		
Mineralogical composition	Elemental iron mass concentration ($\text{MC}_{\text{Fe}\%}$)	Experiment averaged	10%	Uncertainties calculated as discussed in DB17 and C17	
	Iron oxides mass concentration ($\text{MC}_{\text{Fe-ox}\%}$)	Experiment averaged	15%		
	Goethite mass concentration ($\text{MC}_{\text{Goet}\%}$)	Experiment averaged	<10%		
	Hematite mass concentration ($\text{MC}_{\text{Hem}\%}$)	Experiment averaged	<10%		

$$1192 \quad \sigma_f = \sqrt{\sum_{i=1}^n \left(\frac{\partial f}{\partial x_i} \sigma_{x_i} \right)^2}$$

1193
1194
1195
1196
1197
1198
1199
1200
1201
1202

1203
1204
1205

Table 2. Summary of information on the soil samples and sediments used in this study.

Geographical area	Sample	Coordinates	Desert area
Northern Africa – Sahara	Tunisia	33.02°N, 10.67°E	Maouna
	Morocco	31.97°N, 3.28°W	east of Ksar Sahli
	Libya	27.01°N, 14.50°E	Sebha
	Algeria	23.95°N, 5.47°E	Ti-n-Tekraouit
	Mauritania	20.16°N, 12.33°W	east of Aouinet Nchir
Sahel	Niger	13.52°N, 2.63°E	Banizoumbou
	Mali	17.62°N, 4.29°W	Dar el Beida
	Bodélé	17.23°N, 19.03°E	Bodélé depression
Eastern Africa and the Middle East	Ethiopia	7.50°N, 38.65°E	Lake Shala National Park
	Saudi Arabia	27.49°N, 41.98°E	Nefud
	Kuwait	29.42°N, 47.69°E	Kuwaiti
Eastern Asia	Gobi	39.43°N, 105.67°E	Gobi
	Taklimakan	41.83°N, 85.88°E	Taklimakan
North America	Arizona	33.15 °N, 112.08°W	Sonoran
South America	Atacama	23.72°S, 70.40°W	Atacama
	Patagonia	50.26°S, 71.50°W	Patagonia
Southern Africa	Namib–1	21.24°S, 14.99°E	Namib
	Namib–2	19.00°S, 13.00°E	Namib
Australia	Australia	31.33°S, 140.33°E	Strzelecki

1206
1207

Table 3. Chemical characterization of the dust aerosols in the PM_{10.6} size fraction. Column 3 shows MC_{Fe%}, the fractional mass of elemental iron with respect to the total dust mass concentration ($\pm 10\%$ relative uncertainty), and column 4 reports MC_{Fe-ox%}, the mass fraction of iron oxides with respect to the total dust mass concentration ($\pm 15\%$ relative uncertainty) and its speciation in hematite MC_{Hem%} and goethite MC_{Goeth%} ($< \pm 10\%$ relative uncertainty). The iron oxide measurements were not made on the Taklimakan sample. Mean values and standard deviations based on single sample data are reported for the full dataset.

1215

Geographical area	Sample	MC _{Fe%}	MC _{Fe-ox%}	MC _{Hem%}	MC _{Goeth%}
Northern Africa – Sahara	Tunisia	4.1	2.2	1.2	1.1
	Morocco	3.6	1.4	0.4	1.0
	Libya	5.2	3.1	0.9	2.2
	Algeria	6.6	2.7	1.4	1.4
	Mauritania	8.1	3.3	3.3	0.0
Sahel	Niger	6.1	5.8	2.3	3.5
	Mali	6.6	3.7	2.0	1.7
	Bodélé	4.1	0.7	0.7	0.0
Eastern Africa and the Middle East	Ethiopia	6.8	2.0	2.0	0.0
	Saudi Arabia	3.8	2.6	1.8	0.8
	Kuwait	5.0	1.5	1.5	0.0
Eastern Asia	Gobi	4.8	0.9	0.9	0.0
	Taklimakan	5.8	–	–	–
North America	Arizona	5.3	1.5	1.5	0.0
South America	Atacama	4.7	1.6	1.6	0.0
	Patagonia	5.1	1.5	0.9	0.6
Southern Africa	Namib–1	2.4	1.1	0.8	0.3
	Namib–2	10.6	4.8	4.8	0.0
Australia	Australia	7.2	3.6	3.6	0.0
Full dataset mean (st. dev.)		5.6 (1.9)	2.4 (1.4)	1.8 (1.1)	0.7 (1.0)

1216 **Table 4.** Real (n) and imaginary (k) parts of the refractive index estimated for the nineteen analysed
1217 dust samples and mean values calculated for the eight regions and for the full dataset. Data for single
1218 soils are reported as experiment-averaged values and their uncertainty is calculated as indicated in
1219 Table 1. Mean values and standard deviations at each wavelength based on single sample data are
1220 reported for the eight regions and the full dataset. The median and 10% and 90% percentile values are
1221 also reported for the full dataset. For North America and Australia, for which only one dust sample was
1222 analysed, the reported data correspond to the single sample available from these regions. For the real
1223 part, the average over the whole shortwave range (n_{SW}) is indicated.

Sample/Region	n_{SW}	$\sigma_{n_{SW}}$	k							σ_k						
			0.37 μm	0.47 μm	0.52 μm	0.59 μm	0.66 μm	0.88 μm	0.95 μm	0.37 μm	0.47 μm	0.52 μm	0.59 μm	0.66 μm	0.88 μm	0.95 μm
Tunisia	1.51	0.06	0.00 45	0.00 35	0.00 26	0.00 18	0.00 15	0.00 13	0.00 12	0.00 30	0.00 26	0.00 18	0.00 12	0.00 10	0.00 08	0.00 07
Morocco	1.49	0.03	0.00 23	0.00 16	0.00 12	0.00 08	0.00 07	0.00 06	0.00 07	0.00 06	0.00 04	0.00 03	0.00 02	0.00 02	0.00 02	0.00 02
Lybia	1.5	0.04	0.00 29	0.00 19	0.00 14	0.00 07	0.00 06	0.00 07	0.00 07	0.00 06	0.00 04	0.00 02	0.00 01	0.00 02	0.00 02	0.00 02
Algeria	1.52	0.04	0.00 25	0.00 16	0.00 12	0.00 07	0.00 05	0.00 06	0.00 06	0.00 10	0.00 06	0.00 04	0.00 03	0.00 03	0.00 03	0.00 03
Mauritania	1.5	0.03	0.00 43	0.00 33	0.00 26	0.00 14	0.00 13	0.00 10	0.00 10	0.00 10	0.00 09	0.00 08	0.00 03	0.00 03	0.00 04	0.00 03
Northern Africa – Sahara (mean and st. dev.)	1.51	0.03	0.00 33	0.00 24	0.00 18	0.00 11	0.00 09	0.00 08	0.00 08	0.00 10	0.00 10	0.00 07	0.00 05	0.00 04	0.00 03	0.00 03
Niger	1.51	0.04	0.00 88	0.00 61	0.00 48	0.00 34	0.00 31	0.00 28	0.00 21	0.00 43	0.00 31	0.00 23	0.00 18	0.00 15	0.00 10	0.00 13
Mali	1.52	0.05	0.00 48	0.00 38	0.00 30	0.00 23	0.00 24	0.00 21	0.00 21	0.00 08	0.00 06	0.00 04	0.00 03	0.00 03	0.00 03	0.00 03
Bodélé	1.49	0.03	0.00 11	0.00 07	0.00 06	0.00 04	0.00 04	0.00 03	0.00 03	0.00 06	0.00 04	0.00 03	0.00 02	0.00 02	0.00 01	0.00 01
Sahel (mean and st. dev.)	1.51	0.03	0.00 49	0.00 35	0.00 28	0.00 20	0.00 20	0.00 17	0.00 15	0.00 38	0.00 27	0.00 21	0.00 15	0.00 14	0.00 13	0.00 11
Ethiopia	1.55	0.06	0.00 26	0.00 20	0.00 16	0.00 13	0.00 11	0.00 07	0.00 06	0.00 09	0.00 08	0.00 07	0.00 05	0.00 04	0.00 02	0.00 02
Saudi Arabia	1.54	0.06	0.00 28	0.00 21	0.00 15	0.00 07	0.00 06	0.00 06	0.00 06	0.00 06	0.00 05	0.00 04	0.00 02	0.00 01	0.00 01	0.00 01
Kuwait	1.50	0.04	0.00 16	0.00 10	0.00 08	0.00 06	0.00 05	0.00 05	0.00 04	0.00 05	0.00 03	0.00 03	0.00 02	0.00 02	0.00 03	0.00 02
Eastern Africa and the Middle East (mean and st. dev.)	1.53	0.05	0.00 23	0.00 17	0.00 13	0.00 09	0.00 07	0.00 06	0.00 05	0.00 07	0.00 06	0.00 05	0.00 04	0.00 03	0.00 01	0.00 01
Gobi	1.48	0.05	0.00 41	0.00 25	0.00 18	0.00 12	0.00 11	0.00 12	0.00 12	0.00 17	0.00 09	0.00 06	0.00 04	0.00 04	0.00 05	0.00 05
Taklimakan	1.54	0.07	0.00 18	0.00 12	0.00 09	0.00 06	0.00 05	0.00 05	0.00 05	0.00 08	0.00 05	0.00 04	0.00 02	0.00 02	0.00 02	0.00 02
Eastern Asia (mean and st. dev.)	1.51	0.05	0.00 30	0.00 19	0.00 14	0.00 09	0.00 08	0.00 08	0.00 09	0.00 16	0.00 09	0.00 06	0.00 05	0.00 05	0.00 05	0.00 05
Arizona	1.51	0.05	0.00 11	0.00 09	0.00 07	0.00 05	0.00 05	0.00 05	0.00 04	0.00 05	0.00 04	0.00 03	0.00 02	0.00 02	0.00 02	0.00 02
North America (mean and st. dev.)	1.51	0.05	0.00 11	0.00 09	0.00 07	0.00 05	0.00 05	0.00 05	0.00 04	0.00 05	0.00 04	0.00 03	0.00 02	0.00 02	0.00 02	0.00 02
Atacama	1.54	0.07	0.00 16	0.00 15	0.00 12	0.00 08	0.00 06	0.00 06	0.00 06	0.00 05	0.00 04	0.00 03	0.00 02	0.00 02	0.00 02	0.00 02
Patagonia	1.53	0.07	0.00 24	0.00 16	0.00 11	0.00 09	0.00 06	0.00 07	0.00 06	0.00 08	0.00 05	0.00 03	0.00 03	0.00 03	0.00 03	0.00 02
South America (mean and st. dev.)	1.54	0.06	0.00 20	0.00 15	0.00 11	0.00 08	0.00 06	0.00 07	0.00 06	0.00 06	0.00 01	0.00 01	0.00 01	0.00 00	0.00 01	0.00 00
Namib-1	1.53	0.06	0.00 12	0.00 09	0.00 06	0.00 04	0.00 03	0.00 04	0.00 04	0.00 06	0.00 04	0.00 03	0.00 02	0.00 01	0.00 02	0.00 01
Namib-2	1.55	0.07	0.00 72	0.00 54	0.00 44	0.00 25	0.00 18	0.00 14	0.00 14	0.00 27	0.00 19	0.00 16	0.00 09	0.00 07	0.00 06	0.00 06
Southern Africa (mean and st. dev.)	1.54	0.06	0.00 42	0.00 31	0.00 25	0.00 14	0.00 11	0.00 09	0.00 09	0.00 42	0.00 32	0.00 27	0.00 15	0.00 10	0.00 07	0.00 07
Australia	1.54	0.06	0.00 58	0.00 42	0.00 33	0.00 17	0.00 13	0.00 13	0.00 12	0.00 22	0.00 11	0.00 10	0.00 06	0.00 06	0.00 04	0.00 03
Australia (mean and st. dev.)	1.54	0.06	0.00 58	0.00 42	0.00 33	0.00 17	0.00 13	0.00 13	0.00 12	0.00 22	0.00 11	0.00 10	0.00 06	0.00 06	0.00 04	0.00 03
Full dataset (mean and st. dev.)	1.52	0.04	0.00 33	0.00 24	0.00 18	0.00 12	0.00 10	0.00 09	0.00 09	0.00 21	0.00 16	0.00 13	0.00 08	0.00 07	0.00 06	0.00 05
Full dataset median	1.52		0.00 26	0.00 19	0.00 14	0.00 08	0.00 06	0.00 07	0.00 06							
Full dataset 10% percentile	1.49		0.00 12	0.00 09	0.00 07	0.00 05	0.00 04	0.00 04	0.00 04							
Full dataset 90% percentile	1.54		0.00 61	0.00 44	0.00 35	0.00 23	0.00 19	0.00 15	0.00 15							

Table 5. As in Table 4 for the single scattering albedo (SSA) data.

Sample/Region	SSA							σ_{SSA}						
	0.37 μm	0.47 μm	0.52 μm	0.59 μm	0.66 μm	0.88 μm	0.95 μm	0.37 μm	0.47 μm	0.52 μm	0.59 μm	0.66 μm	0.88 μm	0.95 μm
Tunisia	0.85	0.90	0.93	0.95	0.95	0.97	0.97	0.03	0.02	0.02	0.01	0.01	0.01	0.01
Morocco	0.92	0.95	0.96	0.98	0.98	0.98	0.99	0.01	0.01	0.01	0.00	0.00	0.00	0.00
Lybia	0.89	0.93	0.95	0.98	0.98	0.98	0.98	0.02	0.01	0.01	0.00	0.00	0.00	0.00
Algeria	0.87	0.92	0.94	0.97	0.97	0.98	0.98	0.02	0.01	0.01	0.00	0.00	0.00	0.00
Mauritania	0.85	0.90	0.94	0.96	0.97	0.98	0.98	0.02	0.01	0.01	0.01	0.01	0.00	0.00
Northern Africa – Sahara (mean and st. dev.)	0.88	0.92	0.94	0.97	0.97	0.98	0.98	0.03	0.02	0.02	0.01	0.01	0.01	0.01
Niger	0.72	0.85	0.89	0.91	0.92	0.94	0.95	0.09	0.09	0.07	0.05	0.05	0.03	0.02
Mali	0.75	0.85	0.89	0.93	0.95	0.96	0.96	0.04	0.03	0.02	0.02	0.02	0.01	0.01
Bodélé	0.96	0.98	0.98	0.99	0.99	0.99	0.99	0.04	0.02	0.02	0.01	0.01	0.01	0.01
Sahel (mean and st. dev.)	0.81	0.89	0.92	0.94	0.95	0.96	0.97	0.13	0.07	0.05	0.04	0.04	0.03	0.02
Ethiopia	0.80	0.86	0.90	0.92	0.94	0.97	0.97	0.03	0.03	0.02	0.02	0.01	0.01	0.01
Saudi Arabia	0.88	0.93	0.96	0.98	0.98	0.98	0.98	0.03	0.02	0.01	0.01	0.01	0.00	0.00
Kuwait	0.95	0.97	0.98	0.98	0.99	0.99	0.99	0.02	0.01	0.01	0.01	0.01	0.01	0.00
Eastern Africa and the Middle East (mean and st. dev.)	0.88	0.92	0.94	0.96	0.97	0.98	0.98	0.07	0.05	0.04	0.03	0.03	0.01	0.01
Gobi	0.88	0.92	0.94	0.96	0.97	0.97	0.97	0.04	0.03	0.02	0.01	0.01	0.01	0.01
Taklimakan	0.82	0.88	0.92	0.95	0.96	0.96	0.96	0.03	0.02	0.02	0.01	0.01	0.01	0.01
Eastern Asia (mean and st. dev.)	0.85	0.90	0.93	0.96	0.96	0.97	0.97	0.04	0.03	0.02	0.01	0.01	0.01	0.01
Arizona	0.93	0.96	0.97	0.98	0.98	0.99	0.99	0.01	0.01	0.01	0.00	0.00	0.00	0.00
North America (mean and st. dev.)	0.93	0.96	0.97	0.98	0.98	0.99	0.99	0.01	0.01	0.01	0.00	0.00	0.00	0.00
Atacama	0.89	0.93	0.94	0.97	0.97	0.98	0.98	0.03	0.02	0.02	0.01	0.01	0.01	0.01
Patagonia	0.88	0.91	0.94	0.96	0.97	0.98	0.98	0.02	0.02	0.01	0.01	0.01	0.00	0.01
South America (mean and st. dev.)	0.89	0.92	0.94	0.96	0.97	0.98	0.98	0.00	0.01	0.00	0.00	0.00	0.00	0.00
Namib-1	0.91	0.95	0.96	0.98	0.98	0.99	0.99	0.02	0.01	0.01	0.00	0.00	0.00	0.00
Namib-2	0.74	0.82	0.86	0.92	0.94	0.96	0.97	0.03	0.02	0.02	0.01	0.01	0.01	0.01
Southern Africa (mean and st. dev.)	0.83	0.88	0.91	0.95	0.96	0.98	0.98	0.12	0.09	0.07	0.04	0.03	0.02	0.02
Australia	0.70	0.81	0.85	0.91	0.93	0.96	0.97	0.04	0.03	0.02	0.01	0.01	0.01	0.01
Australia (mean and st. dev.)	0.70	0.81	0.85	0.91	0.93	0.96	0.97	0.04	0.03	0.02	0.01	0.01	0.01	0.01
Full dataset (mean and st. dev.)	0.85	0.91	0.93	0.96	0.96	0.97	0.98	0.08	0.05	0.04	0.03	0.02	0.01	0.01
Full dataset median	0.88	0.92	0.94	0.96	0.97	0.98	0.98							
Full dataset 10% percentile	0.74	0.84	0.88	0.92	0.94	0.96	0.96							
Full dataset 90% percentile	0.93	0.96	0.97	0.98	0.99	0.99	0.99							

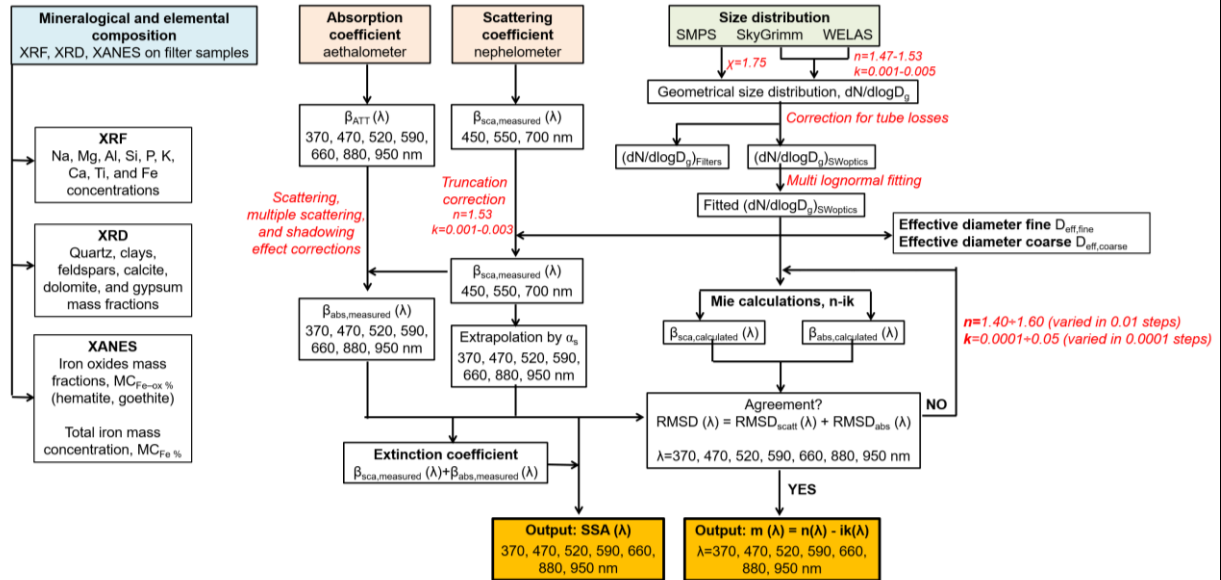
1227 **Table 6.** Results of the linear fit between k and SSA and the mass concentration of iron oxides, $MC_{Fe-ox\%}$,
 1228 hematite, $MC_{Hem\%}$, goethite, $MC_{Goeth\%}$, and elemental iron, $MC_{Fe\%}$ in dust. Column 1 indicates the
 1229 wavelength; $(a \pm \sigma_a)$ indicates the retrieved slope and its estimated uncertainty; $(b \pm \sigma_b)$ indicates the
 1230 retrieved intercept and its estimated uncertainty; R^2 denotes the correlation coefficient and χ^2_{red} is the
 1231 reduced chi-square of the fit.

$k = a MC_{Fe-ox\%} + b$							$SSA = a MC_{Fe-ox\%} + b$						
Wavelength (nm)	$a \pm \sigma_a$	$b \pm \sigma_b$	$R^2 ; \chi^2_{red}$	$a \pm \sigma_a$	$b \pm \sigma_b$	$R^2 ; \chi^2_{red}$	Wavelength (nm)	$a \pm \sigma_a$	$b \pm \sigma_b$	$R^2 ; \chi^2_{red}$	$a \pm \sigma_a$	$b \pm \sigma_b$	$R^2 ; \chi^2_{red}$
370	$(11.9 \pm 2.4) 10^{-4}$	$(2.4 \pm 4.6) 10^{-4}$	0.88 ; 0.6	$(-5.8 \pm 0.8) 10^{-2}$	(1.00 ± 0.02)	0.83 ; 1.7	370	$(9.7 \pm 2.7) 10^{-4}$	$(2.7 \pm 4.0) 10^{-4}$	0.67 ; 1.9	$(-4.4 \pm 0.6) 10^{-2}$	(0.95 ± 0.01)	0.73 ; 3.5
470	$(9.0 \pm 1.7) 10^{-4}$	$(1.7 \pm 3.2) 10^{-4}$	0.89 ; 0.8	$(-3.8 \pm 0.6) 10^{-2}$	(1.00 ± 0.01)	0.78 ; 1.8	470	$(8.3 \pm 1.9) 10^{-4}$	$(1.9 \pm 2.7) 10^{-4}$	0.72 ; 1.9	$(-3.0 \pm 0.4) 10^{-2}$	(0.97 ± 0.01)	0.76 ; 3.2
520	$(6.8 \pm 1.3) 10^{-4}$	$(1.3 \pm 2.4) 10^{-4}$	0.90 ; 0.9	$(-2.9 \pm 0.4) 10^{-2}$	(1.01 ± 0.01)	0.76 ; 2.0	520	$(6.9 \pm 1.5) 10^{-4}$	$(1.5 \pm 2.0) 10^{-4}$	0.74 ; 2.0	$(-2.2 \pm 0.3) 10^{-2}$	(0.98 ± 0.00)	0.78 ; 3.3
590	$(4.5 \pm 0.9) 10^{-4}$	$(0.9 \pm 1.6) 10^{-4}$	0.85 ; 1.4	$(-1.8 \pm 0.3) 10^{-2}$	(1.00 ± 0.01)	0.75 ; 2.3	590	$(3.7 \pm 0.8) 10^{-4}$	$(0.9 \pm 1.2) 10^{-4}$	0.61 ; 2.1	$(-1.3 \pm 0.2) 10^{-2}$	(0.99 ± 0.00)	0.71 ; 2.7
660	$(4.3 \pm 0.8) 10^{-4}$	$(0.8 \pm 1.4) 10^{-4}$	0.81 ; 1.6	$(-1.3 \pm 0.2) 10^{-2}$	(1.00 ± 0.00)	0.75 ; 2.2	660	$(3.7 \pm 0.8) 10^{-4}$	$(0.8 \pm 1.1) 10^{-4}$	0.51 ; 2.6	$(-0.9 \pm 0.2) 10^{-2}$	(0.99 ± 0.00)	0.62 ; 2.5
880	$(3.4 \pm 0.6) 10^{-4}$	$(0.6 \pm 1.2) 10^{-4}$	0.79 ; 1.0	$(-0.76 \pm 0.16) 10^{-2}$	(1.00 ± 0.00)	0.79 ; 1.4	880	$(2.9 \pm 0.7) 10^{-4}$	$(0.7 \pm 1.1) 10^{-4}$	0.43 ; 2.1	$(-0.6 \pm 0.1) 10^{-2}$	(0.99 ± 0.00)	0.57 ; 1.8
950	$(3.2 \pm 0.6) 10^{-4}$	$(0.6 \pm 1.0) 10^{-4}$	0.77 ; 1.1	$(-0.62 \pm 0.13) 10^{-2}$	(0.99 ± 0.00)	0.78 ; 1.1	950	$(2.6 \pm 0.6) 10^{-4}$	$(0.6 \pm 0.9) 10^{-4}$	0.46 ; 2.1	$(-0.5 \pm 0.1) 10^{-2}$	(0.99 ± 0.00)	0.49 ; 1.7
$k = a MC_{Hem\%} + b$							$SSA = a MC_{Hem\%} + b$						
Wavelength (nm)	$a \pm \sigma_a$	$b \pm \sigma_b$	$R^2 ; \chi^2_{red}$	$a \pm \sigma_a$	$b \pm \sigma_b$	$R^2 ; \chi^2_{red}$	Wavelength (nm)	$a \pm \sigma_a$	$b \pm \sigma_b$	$R^2 ; \chi^2_{red}$	$a \pm \sigma_a$	$b \pm \sigma_b$	$R^2 ; \chi^2_{red}$
370	$(9.0 \pm 2.5) 10^{-4}$	$(2.5 \pm 2.2) 10^{-4}$	0.47 ; 1.8	$(-13.4 \pm 6.9) 10^{-3}$	(0.90 ± 0.01)	0.32 ; 6.8	370	$(6.0 \pm 1.4) 10^{-4}$	$(1.4 \pm 0.7) 10^{-4}$	0.60 ; 1.5	$(-2.7 \pm 0.4) 10^{-2}$	(1.02 ± 0.02)	0.67 ; 3.1
470	$(5.5 \pm 1.7) 10^{-4}$	$(1.7 \pm 1.5) 10^{-4}$	0.43 ; 2.3	$(-8.3 \pm 4.7) 10^{-3}$	(0.94 ± 0.00)	0.21 ; 6.2	470	$(4.7 \pm 1.0) 10^{-4}$	$(1.0 \pm 0.5) 10^{-4}$	0.62 ; 1.7	$(-1.8 \pm 0.3) 10^{-2}$	(1.02 ± 0.01)	0.72 ; 2.8
520	$(3.4 \pm 1.1) 10^{-4}$	$(1.1 \pm 1.2) 10^{-4}$	0.41 ; 2.5	$(-4.9 \pm 3.2) 10^{-3}$	(0.96 ± 0.00)	0.17 ; 6.4	520	$(3.9 \pm 0.8) 10^{-4}$	$(0.8 \pm 3.9) 10^{-4}$	0.65 ; 1.6	$(-1.3 \pm 0.2) 10^{-2}$	(1.01 ± 0.01)	0.72 ; 2.9
590	$(0.5 \pm 0.6) 10^{-4}$	$(0.6 \pm 0.8) 10^{-4}$	0.50 ; 3.2	$(0.9 \pm 2.0) 10^{-3}$	(0.97 ± 0.00)	0.23 ; 5.5	590	$(2.5 \pm 0.5) 10^{-4}$	$(0.5 \pm 2.4) 10^{-4}$	0.56 ; 1.7	$(-0.8 \pm 0.1) 10^{-2}$	(1.01 ± 0.01)	0.70 ; 2.4
660	$(2.2 \pm 0.8) 10^{-4}$	$(0.8 \pm 0.7) 10^{-4}$	0.55 ; 3.6	$(0.2 \pm 1.6) 10^{-3}$	(0.98 ± 0.00)	0.34 ; 4.4	660	$(2.0 \pm 0.4) 10^{-4}$	$(0.4 \pm 1.7) 10^{-4}$	0.48 ; 1.9	$(-0.5 \pm 0.1) 10^{-2}$	(1.00 ± 0.00)	0.62 ; 2.0
880	$(2.6 \pm 0.8) 10^{-4}$	$(0.8 \pm 0.6) 10^{-4}$	0.62 ; 2.4	$(-1.1 \pm 1.4) 10^{-3}$	(0.98 ± 0.00)	0.47 ; 3.0	880	$(1.8 \pm 0.4) 10^{-4}$	$(0.4 \pm 2.0) 10^{-4}$	0.40 ; 1.8	$(-0.4 \pm 0.1) 10^{-2}$	(1.00 ± 0.00)	0.54 ; 1.6
950	$(2.6 \pm 0.8) 10^{-4}$	$(0.8 \pm 0.6) 10^{-4}$	0.55 ; 2.5	$(-2.1 \pm 1.4) 10^{-3}$	(0.98 ± 0.00)	0.54 ; 2.6	950	$(1.4 \pm 0.3) 10^{-4}$	$(0.3 \pm 1.4) 10^{-4}$	0.45 ; 2.0	$(-0.3 \pm 0.1) 10^{-2}$	(1.00 ± 0.00)	0.49 ; 1.5
$k = a MC_{Goeth\%} + b$							$SSA = a MC_{Goeth\%} + b$						
Wavelength (nm)	$a \pm \sigma_a$	$b \pm \sigma_b$	$R^2 ; \chi^2_{red}$	$a \pm \sigma_a$	$b \pm \sigma_b$	$R^2 ; \chi^2_{red}$	Wavelength (nm)	$a \pm \sigma_a$	$b \pm \sigma_b$	$R^2 ; \chi^2_{red}$	$a \pm \sigma_a$	$b \pm \sigma_b$	$R^2 ; \chi^2_{red}$
370	$(6.0 \pm 1.4) 10^{-4}$	$(1.4 \pm 0.7) 10^{-4}$	0.60 ; 1.5	$(-2.7 \pm 0.4) 10^{-2}$	(1.02 ± 0.02)	0.67 ; 3.1	370	$(6.0 \pm 1.4) 10^{-4}$	$(1.4 \pm 0.7) 10^{-4}$	0.60 ; 1.5	$(-2.7 \pm 0.4) 10^{-2}$	(1.02 ± 0.02)	0.67 ; 3.1
470	$(4.7 \pm 1.0) 10^{-4}$	$(1.0 \pm 0.5) 10^{-4}$	0.62 ; 1.7	$(-1.8 \pm 0.3) 10^{-2}$	(1.02 ± 0.01)	0.72 ; 2.8	470	$(4.7 \pm 1.0) 10^{-4}$	$(1.0 \pm 0.5) 10^{-4}$	0.62 ; 1.7	$(-1.8 \pm 0.3) 10^{-2}$	(1.02 ± 0.01)	0.72 ; 2.8
520	$(3.9 \pm 0.8) 10^{-4}$	$(0.8 \pm 3.9) 10^{-4}$	0.65 ; 1.6	$(-1.3 \pm 0.2) 10^{-2}$	(1.01 ± 0.01)	0.72 ; 2.9	520	$(3.9 \pm 0.8) 10^{-4}$	$(0.8 \pm 3.9) 10^{-4}$	0.65 ; 1.6	$(-1.3 \pm 0.2) 10^{-2}$	(1.01 ± 0.01)	0.72 ; 2.9
590	$(2.5 \pm 0.5) 10^{-4}$	$(0.5 \pm 2.4) 10^{-4}$	0.56 ; 1.7	$(-0.8 \pm 0.1) 10^{-2}$	(1.01 ± 0.01)	0.70 ; 2.4	590	$(2.5 \pm 0.5) 10^{-4}$	$(0.5 \pm 2.4) 10^{-4}$	0.56 ; 1.7	$(-0.8 \pm 0.1) 10^{-2}$	(1.01 ± 0.01)	0.70 ; 2.4
660	$(2.0 \pm 0.4) 10^{-4}$	$(0.4 \pm 1.7) 10^{-4}$	0.48 ; 1.9	$(-0.5 \pm 0.1) 10^{-2}$	(1.00 ± 0.00)	0.62 ; 2.0	660	$(2.0 \pm 0.4) 10^{-4}$	$(0.4 \pm 1.7) 10^{-4}$	0.48 ; 1.9	$(-0.5 \pm 0.1) 10^{-2}$	(1.00 ± 0.00)	0.62 ; 2.0
880	$(1.8 \pm 0.4) 10^{-4}$	$(0.4 \pm 2.0) 10^{-4}$	0.40 ; 1.8	$(-0.4 \pm 0.1) 10^{-2}$	(1.00 ± 0.00)	0.54 ; 1.6	880	$(1.8 \pm 0.4) 10^{-4}$	$(0.4 \pm 2.0) 10^{-4}$	0.40 ; 1.8	$(-0.4 \pm 0.1) 10^{-2}$	(1.00 ± 0.00)	0.54 ; 1.6
950	$(1.4 \pm 0.3) 10^{-4}$	$(0.3 \pm 1.4) 10^{-4}$	0.45 ; 2.0	$(-0.3 \pm 0.1) 10^{-2}$	(1.00 ± 0.00)	0.49 ; 1.5	950	$(1.4 \pm 0.3) 10^{-4}$	$(0.3 \pm 1.4) 10^{-4}$	0.45 ; 2.0	$(-0.3 \pm 0.1) 10^{-2}$	(1.00 ± 0.00)	0.49 ; 1.5
$k = a MC_{Fe\%} + b$							$SSA = a MC_{Fe\%} + b$						
Wavelength (nm)	$a \pm \sigma_a$	$b \pm \sigma_b$	$R^2 ; \chi^2_{red}$	$a \pm \sigma_a$	$b \pm \sigma_b$	$R^2 ; \chi^2_{red}$	Wavelength (nm)	$a \pm \sigma_a$	$b \pm \sigma_b$	$R^2 ; \chi^2_{red}$	$a \pm \sigma_a$	$b \pm \sigma_b$	$R^2 ; \chi^2_{red}$
370	$(6.0 \pm 1.4) 10^{-4}$	$(1.4 \pm 0.7) 10^{-4}$	0.60 ; 1.5	$(-2.7 \pm 0.4) 10^{-2}$	(1.02 ± 0.02)	0.67 ; 3.1	370	$(6.0 \pm 1.4) 10^{-4}$	$(1.4 \pm 0.7) 10^{-4}$	0.60 ; 1.5	$(-2.7 \pm 0.4) 10^{-2}$	(1.02 ± 0.02)	0.67 ; 3.1
470	$(4.7 \pm 1.0) 10^{-4}$	$(1.0 \pm 0.5) 10^{-4}$	0.62 ; 1.7	$(-1.8 \pm 0.3) 10^{-2}$	(1.02 ± 0.01)	0.72 ; 2.8	470	$(4.7 \pm 1.0) 10^{-4}$	$(1.0 \pm 0.5) 10^{-4}$	0.62 ; 1.7	$(-1.8 \pm 0.3) 10^{-2}$	(1.02 ± 0.01)	0.72 ; 2.8
520	$(3.9 \pm 0.8) 10^{-4}$	$(0.8 \pm 3.9) 10^{-4}$	0.65 ; 1.6	$(-1.3 \pm 0.2) 10^{-2}$	(1.01 ± 0.01)	0.72 ; 2.9	520	$(3.9 \pm 0.8) 10^{-4}$	$(0.8 \pm 3.9) 10^{-4}$	0.65 ; 1.6	$(-1.3 \pm 0.2) 10^{-2}$	(1.01 ± 0.01)	0.72 ; 2.9
590	$(2.5 \pm 0.5) 10^{-4}$	$(0.5 \pm 2.4) 10^{-4}$	0.56 ; 1.7	$(-0.8 \pm 0.1) 10^{-2}$	(1.01 ± 0.01)	0.70 ; 2.4	590	$(2.5 \pm 0.5) 10^{-4}$	$(0.5 \pm 2.4) 10^{-4}$	0.56 ; 1.7	$(-0.8 \pm 0.1) 10^{-2}$	(1.01 ± 0.01)	0.70 ; 2.4
660	$(2.0 \pm 0.4) 10^{-4}$	$(0.4 \pm 1.7) 10^{-4}$	0.48 ; 1.9	$(-0.5 \pm 0.1) 10^{-2}$	(1.00 ± 0.00)	0.62 ; 2.0	660	$(2.0 \pm 0.4) 10^{-4}$	$(0.4 \pm 1.7) 10^{-4}$	0.48 ; 1.9	$(-0.5 \pm 0.1) 10^{-2}$	(1.00 ± 0.00)	0.62 ; 2.0
880	$(1.8 \pm 0.4) 10^{-4}$	$(0.4 \pm 2.0) 10^{-4}$	0.40 ; 1.8	$(-0.4 \pm 0.1) 10^{-2}$	(1.00 ± 0.00)	0.54 ; 1.6	880	$(1.8 \pm 0.4) 10^{-4}$	$(0.4 \pm 2.0) 10^{-4}$	0.40 ; 1.8	$(-0.4 \pm 0.1) 10^{-2}$	(1.00 ± 0.00)	0.54 ; 1.6
950	$(1.4 \pm 0.3) 10^{-4}$	$(0.3 \pm 1.4) 10^{-4}$	0.45 ; 2.0	$(-0.3 \pm 0.1) 10^{-2}$	(1.00 ± 0.00)	0.49 ; 1.5	950	$(1.4 \pm 0.3) 10^{-4}$	$(0.3 \pm 1.4) 10^{-4}$	0.45 ; 2.0	$(-0.3 \pm 0.1) 10^{-2}$	(1.00 ± 0.00)	0.49 ; 1.5

1232
 1233
 1234
 1235
 1236
 1237
 1238
 1239
 1240

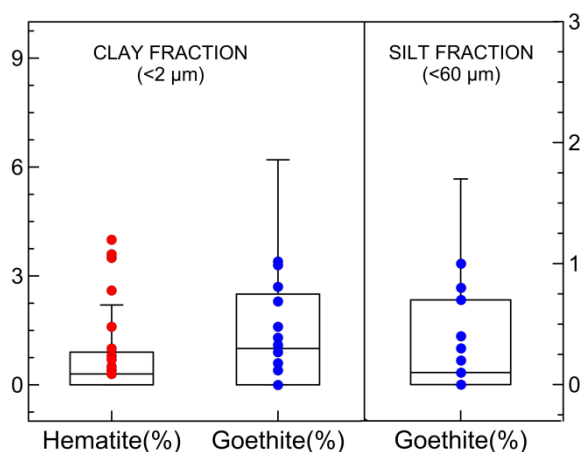
1241 **Figure 1.** Flowchart illustrating the procedure for data treatment and retrieval of physical and chemical
 1242 (size, composition) and spectral optical properties (single scattering albedo, SSA, and complex refrac-
 1243 tive index) of mineral dust aerosols. In red we mention the different corrections performed and the
 1244 values adopted in the calculations.

1245



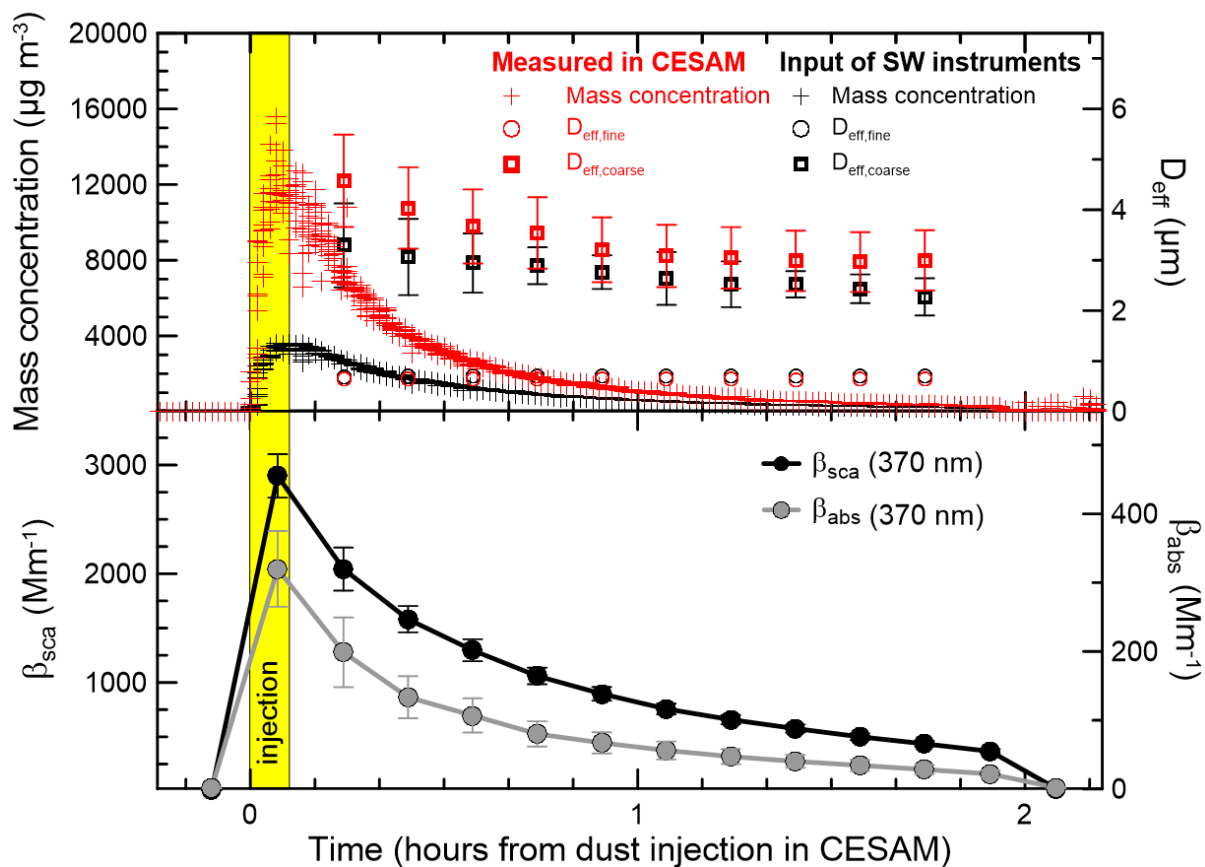
1247
1248

1249 **Figure 2.** Box and whisker plot showing the full variability of hematite and goethite mass fractions in
 1250 the soils for the clay-sized (<2 μm diameter) and silt-sized (<60 μm diameter) fractions as retrieved
 1251 from the global soil mineralogical database by Journet et al. (2014). The box and whisker plot include
 1252 data for the nine desert source areas depicted in Ginoux et al. (2012) and DB17 (Northern Africa, Sahel,
 1253 Eastern Africa and the Middle East, Central Asia, Eastern Asia, North America, South America, South-
 1254 ern Africa, and Australia). Dots indicate hematite and goethite content in clay-sized and silt-sized soils
 1255 (always from Journet et al.) extracted in correspondence to the geographical coordinates where the
 1256 nineteen soils used in the CESAM experiments were collected. The Journet et al. database assumes
 1257 that the iron oxides in the silt fraction consist only of goethite.
 1258



1259
 1260
 1261
 1262
 1263
 1264
 1265
 1266
 1267
 1268
 1269
 1270
 1271
 1272
 1273
 1274
 1275
 1276
 1277
 1278

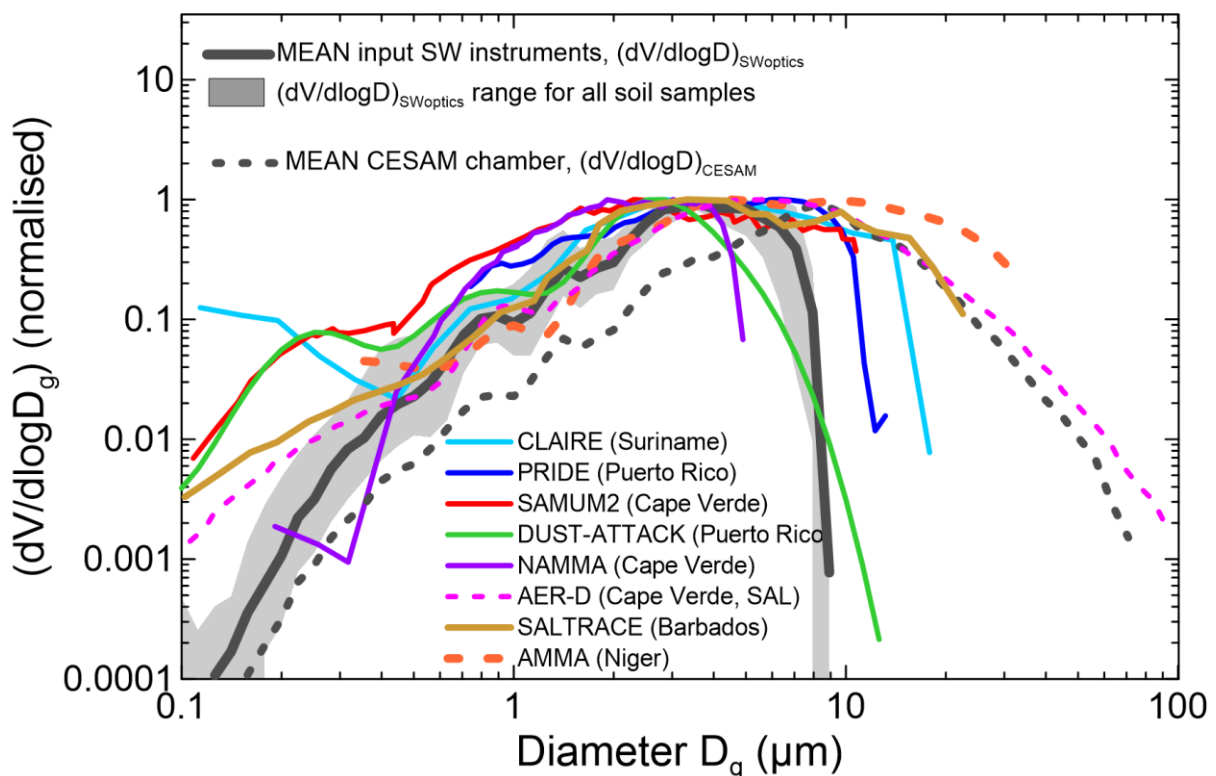
1279 **Figure 3.** Top panel: time series of the aerosol mass concentration (cross symbols) and effective fine
 1280 ($D_{eff,fine}$, open dots) and coarse diameter ($D_{eff,coarse}$, open squares) measured inside the CESAM cham-
 1281 ber (red symbols) and at the input of the SW instruments (black symbols) for one experiment (Morocco
 1282 dust). Bottom panel: time series of the scattering β_{sca} and absorption β_{abs} coefficients at 370 nm for the
 1283 same experiment. Mass concentrations are reported as 6-sec data, while all other quantities are 10-
 1284 min averages.
 1285



1286
 1287
 1288
 1289
 1290
 1291
 1292
 1293
 1294
 1295
 1296
 1297
 1298
 1299
 1300
 1301

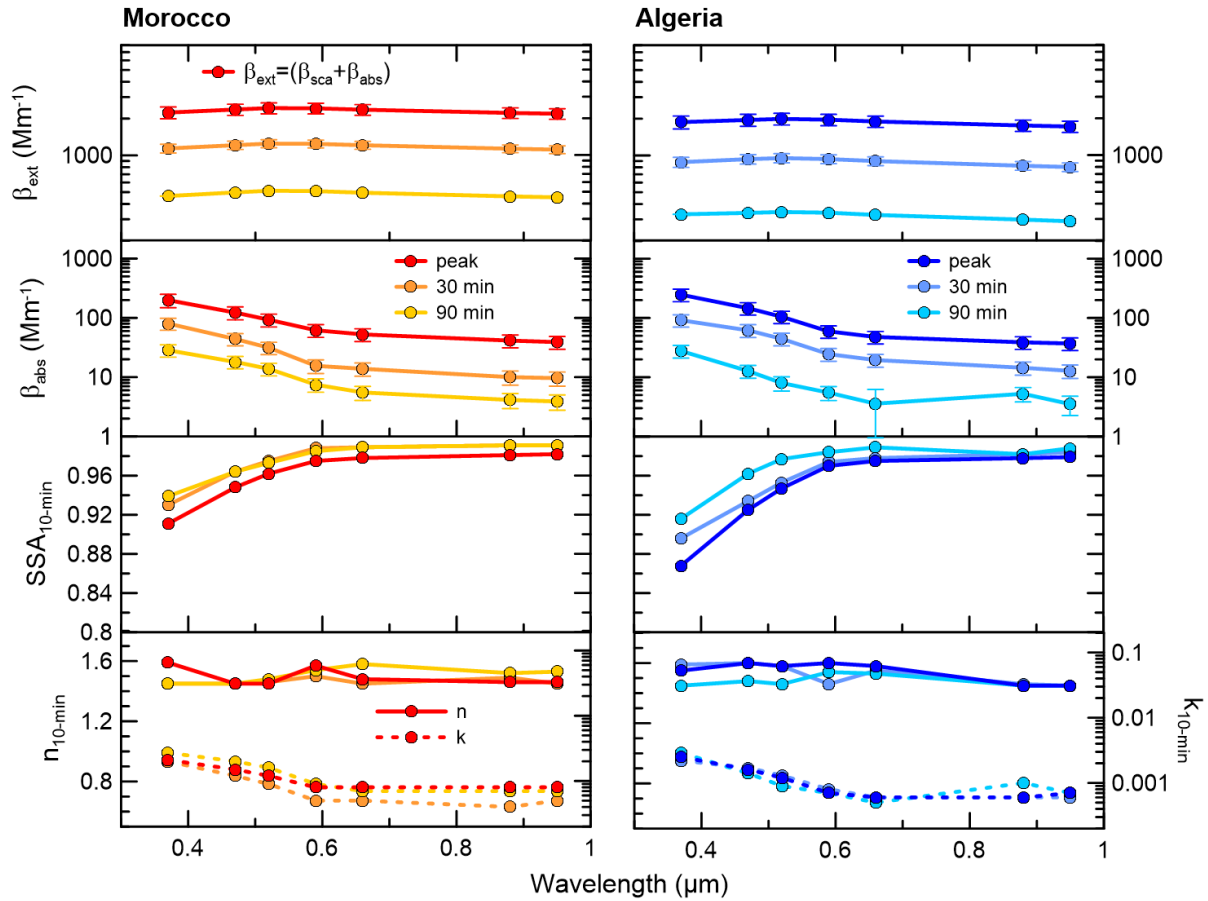
1302 **Figure 4.** Comparison of dust size distributions sensed by the SW optical instruments (behind the SW
 1303 instruments inlet $(dV/d\log D_g)_{SWoptics}$), with field data for long-range transported dust. The thick black line
 1304 represents the mean value of $(dV/d\log D_g)_{SWoptics}$ at the peak of the dust injection in CESAM for experi-
 1305 ments with the different samples. The grey shaded area indicates the range of $(dV/d\log D_g)_{SWoptics}$ for all
 1306 samples. The dotted black line shows the average of the dust size distribution at the peak of the injection
 1307 inside the CESAM chamber from DB17. Field data are from: Formenti et al. (2001) (CLAIRE campaign
 1308 in Suriname, South America), Maring et al. (2003) and Denjean et al. (2016b) (PRIDE and DUST-
 1309 ATTACK campaigns in Puerto Rico, Caraibes), Müller et al. (2011), Chen et al. (2011) and Ryder et al.
 1310 (2018) (SAMUM2, NAMMA, and AER-D campaigns in Cape Verde, eastern Atlantic), and Weinzierl et
 1311 al. (2017) (SALTRACE campaign, data from Barbados). For comparison, data taken close to the source
 1312 in Niger from Formenti et al. (2011) during the AMMA campaign are also shown. SAL stands for Sa-
 1313 haran Air Layer. All data are reported as volume size distributions normalised at the maximum.
 1314 *(The different acronyms spell out as: AER-D= AERosol Properties – Dust; AMMA = African Monsoon*
 1315 *Multidisciplinary Analysis; CLARE= Cooperative LBA Airborne Regional Experiment; DUST-ATTACK+*
 1316 *Dust Aging and Transport from Africa to the Caribbean; NAMMA = NASA African Monsoon Multidisci-*
 1317 *plinary Analysis; PRIDE = Puerto Rico Dust Experiment; SALTRACE= Saharan Aerosol Long-range*
 1318 *Transport and Aerosol-Cloud-Interaction Experiment; SAMUM = Saharan Mineral Dust Experiment).*

1319
 1320



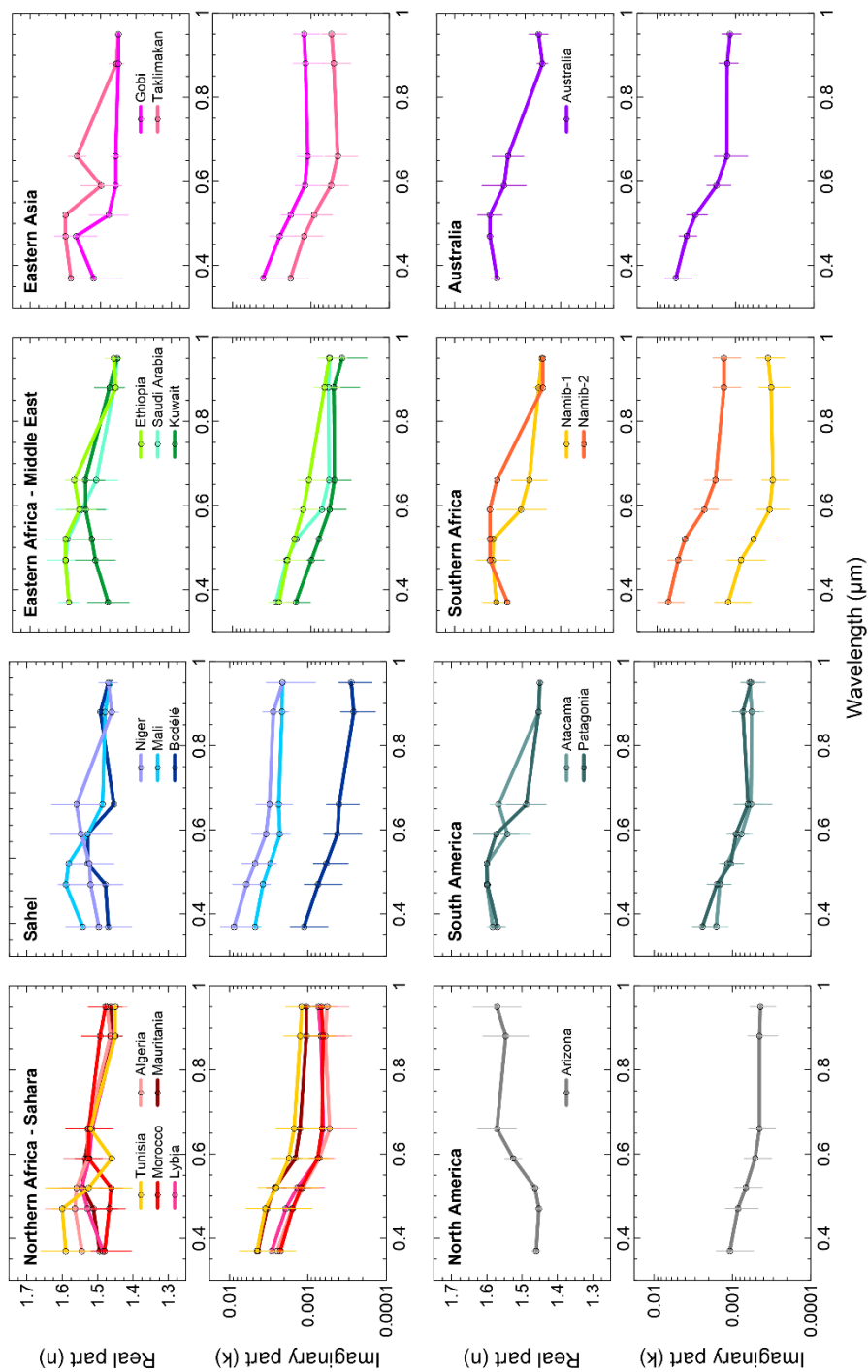
1321
 1322
 1323
 1324
 1325

1326 **Figure 5.** Spectral extinction coefficient, absorption coefficient, SSA, and real (n) and imaginary (k)
 1327 parts of the refractive index at the peak of the dust injection in the chamber and after 30 and 90 minutes
 1328 for Morocco and Algeria dust samples. Data are reported at the seven aethalometer wavelengths (370,
 1329 470, 520, 590, 660, 880, and 950 nm) as 10-min averages. In the top panel we report the extinction
 1330 calculated as the sum of scattering and absorption coefficients. For the sake of clarity error bars are not
 1331 shown for SSA, n , and k data.
 1332



1333
 1334
 1335
 1336
 1337
 1338
 1339
 1340
 1341
 1342
 1343
 1344
 1345

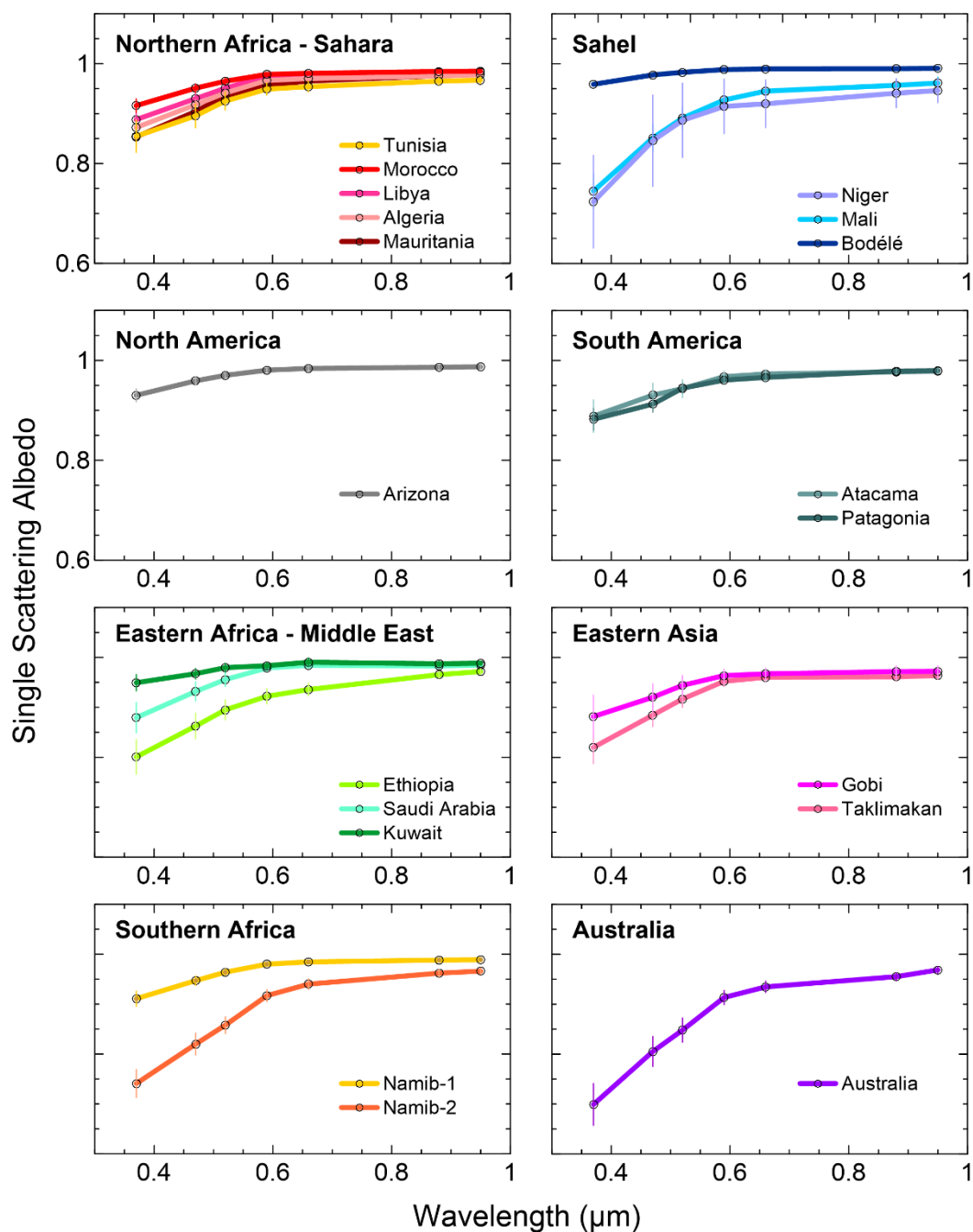
1346 **Figure 6.** Real (n) and imaginary (k) parts of the dust complex refractive index at seven wavelengths
 1347 between 370 and 950 nm obtained for the 19 aerosol samples analyzed in this study. Data correspond
 1348 to the time average of the 10 min values obtained between the peak of the injection and 120 min later.
 1349 The error bar corresponds to the absolute uncertainty in n and k , estimated to be <8% for n and between
 1350 13 and 75 % for k .
 1351



1352
 1353
 1354

1355 **Figure 7.** Single scattering albedo (SSA) at seven wavelengths between 370 and 950 nm obtained for
 1356 the 19 aerosol samples analyzed in this study. Data correspond for each sample (with the exception of
 1357 Tunisia and Namib-2, see Sect. 3.1) to the fit of the 10 min values of β_{sca} versus β_{abs} , and the uncertainty
 1358 is between 1% and 12% at 370 nm and between 1% and 3% at 950 nm.

1359



1360

1361

1362

1363

1364

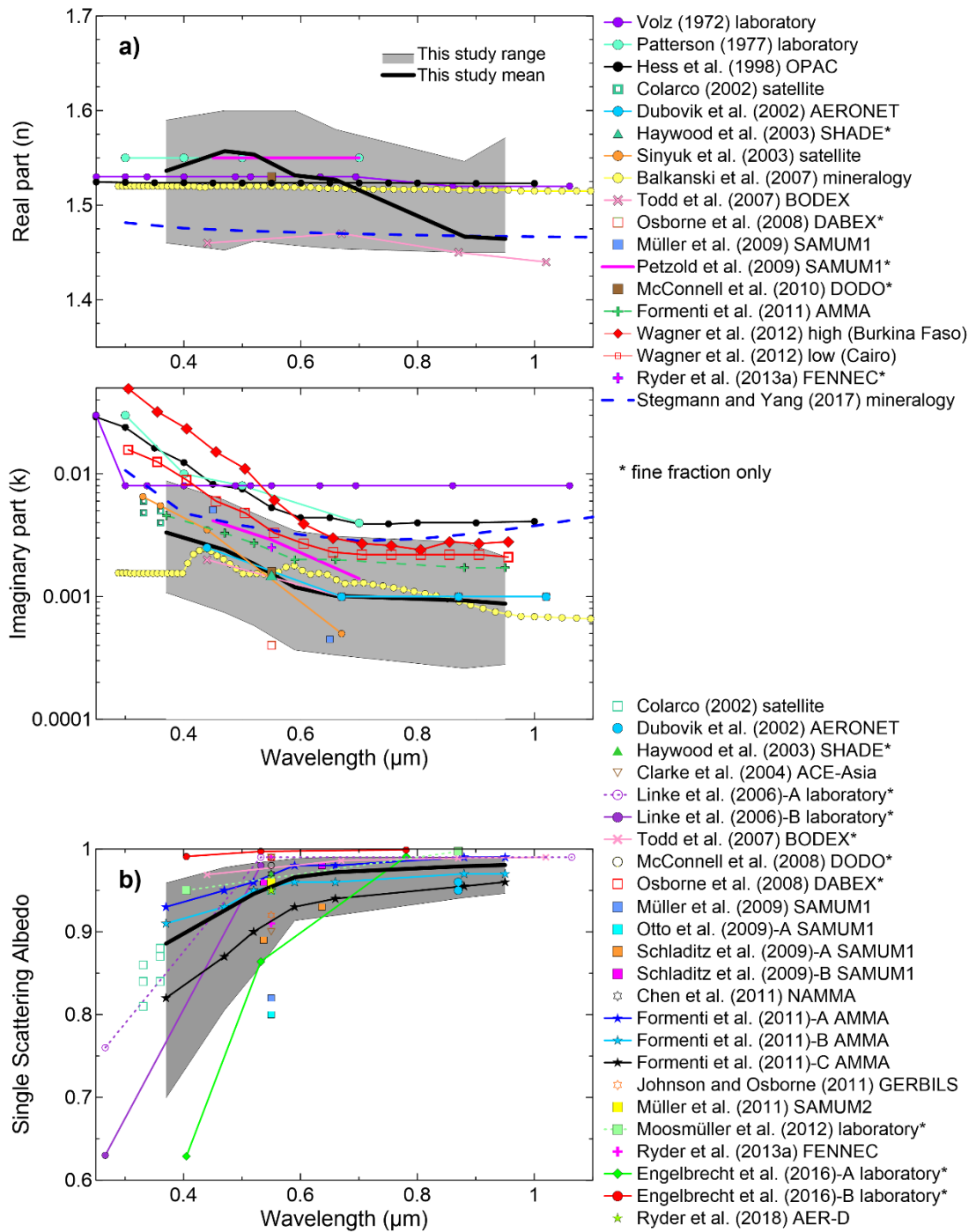
1365 **Figure 8.** Comparison of results obtained in this study with literature–compiled values of the (a) dust
1366 real and imaginary parts of the refractive index (n , k) and (b) single scattering albedo (SSA) in the SW
1367 spectral range. The regions in grey indicate the full range of variability obtained in this study, and the
1368 black thick lines are the means of n , k and SSA obtained for the different aerosol samples. Literature
1369 values include estimates from ground–based and aircraft observations during field campaigns, labora-
1370 tory studies, AERONET inversions, and estimates from dust mineralogical composition. Data are in
1371 some cases for the full dust size distribution, while in other only the fine fraction below about 2 μm is
1372 represented (identified with *).

1373 The main provenance of the dust and datasets from the literature is provided in the following: Volz et
1374 al. (1972) is data for rainout dust collected in Germany; Patterson et al. (1977) is Saharan dust; Hess
1375 et al. (1998) is data from the OPAC database; Colarco et al. (2002) is data for dust from Dakar, Sal,
1376 and Tenerife; Dubovik et al. (2002) included data from Bahrain–Persian Gulf and Solar Village–Saudi
1377 Arabia AERONET stations; Haywood et al. (2003) is dust from Mauritania; Sinyuk et al. (2003) is data
1378 from Cape Verde, Dakar, and Burkina Faso; Clarke et al. (2004) is Asian dust offshore of China, Japan,
1379 and Korea; Linke et al. (2006)–A is dust from Cairo; Linke et al. (2006)–B is dust from Morocco; Bal-
1380 kanski et al (2007) is calculated from mineralogical composition assuming a 1.5% hematite mass frac-
1381 tion in dust; Todd et al. (2007) is from Bodélé; Osborne et al. (2008) is from Niger; Otto et al. (2009),
1382 Petzold et al. (2009), Schladitz et al. (2009), and Muller et al. (2010, 2011) is dust originated mostly in
1383 Morocco; McConnell et al. (2008, 2010) is dust from Niger/Senegal; Chen et al. (2011) is dust from
1384 Western Sahara; Formenti et al. (2011) in the k plot is an average of airborne observations for the
1385 AMMA campaign in Niger, while for the SSA plot, Formenti et al. (2011)–A is from observations in the
1386 Saharan Air Layer, –B is from Bodélé/Sudan, and –C is a Sahelian uplift episode; Johnson et al. (2011)
1387 is dust from Western Sahara; Moosmüller et al. (2012) analysed samples from Middle East, Mali and
1388 Spain, and here we report the average of their obtained values; Wagner et al. (2012) obtained k values
1389 for several samples from Burkina Faso, Cairo and the SAMUM campaign and here we report the values
1390 for the maximum of their spectral k (Burkina Faso) and the minimum (Cairo); Ryder et al. (2013) is dust
1391 from Western Sahara and Mauritania and we report in both k and SSA plots the average of their obser-
1392 vations; Engelbrecht et al. (2016) analysed many dust samples from all over the world, here we report
1393 their estimated minimum and maximum of the dust SSA that are –A from California and –B from the
1394 Etosha Pan in Namibia; Stegmann and Yang (2017) modelled the refractive index of dust based on
1395 assumed mineralogical compositions typical for Northern and Southern Sahara and Western and East-
1396 ern Asia dust, and here we report the average of their results for both n and k . Uncertainties in the field
1397 observations have been omitted for the sake of clarity. The legend identifies the line styles used in the
1398 plots.

1399 *(The different acronyms spell out as (see also the caption of Fig. 4): AERONET = Aerosol Robotic*
1400 *Network; OPAC = Optical Properties of Aerosols and Clouds; SHADE = Saharan Dust Experiment;*
1401 *BODEX = The Bodélé Dust Experiment; DABEX = Dust and Biomass Experiment; SAMUM1 and*
1402 *SAMUM2 refers to the two SAMUM campaigns in Morocco and Cape Verde, respectively, SAMUM =*
1403 *Saharan Mineral Dust Experiment; DODO = Dust Outflow and Deposition to the Ocean; ACE–Asia =*

1404 Asian Pacific Regional Aerosol Characterization Experiment; GERBILS = Geostationary Earth Radiation Budget Intercomparison of Longwave and Shortwave radiation).

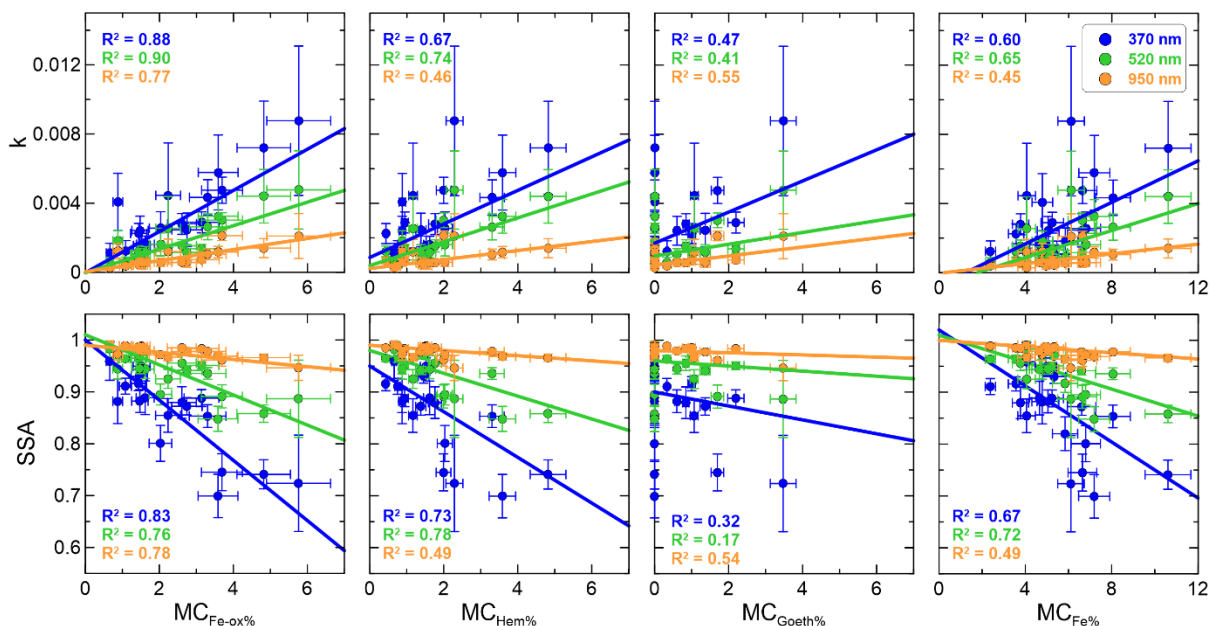
1405
1406
1407



1408
1409
1410
1411
1412
1413
1414

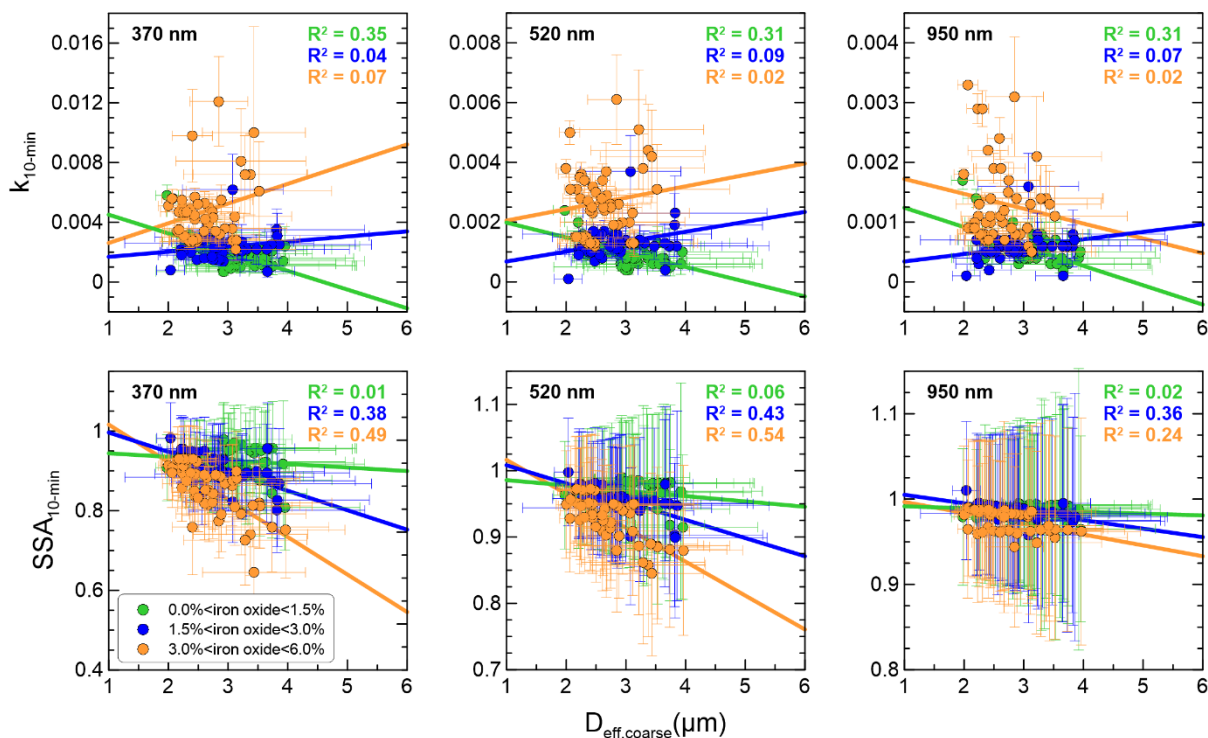
1415 **Figure 9.** Experiment-averaged imaginary part of the refractive index (k , top panels) and single scat-
 1416 tering albedo (SSA, bottom panels) at 370, 520, and 950 nm versus the mass concentration of iron
 1417 oxides ($MC_{Fe-ox\%}$), hematite ($MC_{Hem\%}$), goethite ($MC_{Goeth\%}$), and elemental iron ($MC_{Fe\%}$) measured for
 1418 the different dust samples analysed in this study. The calculated linear fit regression lines are shown,
 1419 together with the correlation coefficients of the fits (R^2). The legend indicates the line styles used in the
 1420 plots. Data for the Taklimakan sample were excluded from the k and SSA plots versus $MC_{Fe-ox\%}$,
 1421 $MC_{Hem\%}$, and $MC_{Goeth\%}$ due to the absence of data for this sample.

1422
 1423
 1424



1425
 1426
 1427
 1428
 1429
 1430
 1431
 1432
 1433
 1434
 1435
 1436
 1437
 1438
 1439
 1440
 1441
 1442
 1443

1444 **Figure 10.** 10-min averaged imaginary refractive index ($k_{10\text{-min}}$, top panels) and single scattering albedo ($SSA_{10\text{-min}}$, bottom panels) at 370, 520, and 950 nm versus effective coarse diameter ($D_{\text{eff,coarse}}$) esti-
 1445 mated at the input of the SW instruments. Data were classified in three classes based on the iron oxide
 1446 content of the dust samples. The linear fit curves and the correlation coefficients for the linear regression
 1447 fits for each dataset are also reported. The legend identifies the line styles used in the plots.
 1448
 1449
 1450



1451